



Mesoscopic modeling of the uniaxial compression and recovery of vertically aligned carbon nanotube forests

Bernard K. Wittmaack^a, Alexey N. Volkov^b, Leonid V. Zhigilei^{a,*}

^a Department of Materials Science and Engineering, University of Virginia, 395 McCormick Road, Charlottesville, VA, 22904-4745, USA

^b Department of Mechanical Engineering, University of Alabama, Hardaway Hall, 7th Avenue, Tuscaloosa, AL, 35487, USA

ARTICLE INFO

Article history:

Received 2 December 2017

Received in revised form

9 March 2018

Accepted 13 March 2018

Available online 14 March 2018

ABSTRACT

Vertically aligned carbon nanotube (VACNT) arrays or “forests” represent a promising class of mechanically strong and resilient lightweight materials, capable of supporting large reversible deformation and absorbing mechanical energy. The mechanical response of VACNT forests to uniaxial compression is defined by various factors, including the material microstructure, its density, height, rate of deformation, and the nature of interaction between carbon nanotubes (CNTs) and the compressing indenter. In this paper, we use a coarse-grained mesoscopic model to simulate the uniaxial compression of VACNT samples with different densities and microstructures (bundle size distribution and degree of nanotube alignment) to obtain a clear microscopic picture of the structural changes in networks of interconnected CNT bundles undergoing mechanical deformation. The key factors responsible for the coordinated buckling of CNTs, reversible and irreversible modes of deformation in VACNT arrays undergoing uniaxial compression, as well as hysteresis behavior in VACNT arrays subjected to five loading–unloading cycles are investigated in the simulations. The simulation results reveal the important role of the collective buckling of CNTs across bundle cross-sections as well as a complex deformation behavior of VACNT arrays defined by an interplay of different modes of bundle deformation. The loading rate and the CNT attachment to the indenter are found to have a strong effect on the deformation mechanisms and the overall mechanical behavior of VACNT forests. A good agreement with experimental data from *in situ* mechanical tests is observed for the general trends and magnitudes of loss coefficients predicted in the simulations. The forest morphology can strongly alter the mechanical behavior of VACNT arrays with nominally the same general characteristics, such as CNT radius, length, and material density, thus suggesting the opportunity for substantial enhancement of the mechanical properties through the microstructure modification.

© 2018 Elsevier Ltd. All rights reserved.

1. Introduction

Vertically aligned carbon nanotube (VACNT) arrays, also known as carbon nanotube (CNT) “forests,” [1] hold significant promise as mechanically strong and resilient lightweight materials. When subjected to compressive loading, VACNT arrays exhibit a number of fascinating properties caused by collective interactions among CNTs organized into anisotropic networks of bundles, such as collective or coordinate buckling [2,3] leading to the formation of microscopic wavy patterns on surfaces of the deformed samples and enabling compression up to 85% strain for thousands of cycles

with almost complete recovery after unloading [2]. The impressive ability of VACNT forests to withstand repeated loading while maintaining high uniaxial stress makes them ideally suited for use as light-weight, energy absorbing materials, cushions, and pressure sensors [2,4–8]. Compared with conventional low-density foams, CNT materials often exhibit a superior combination of compressive strength, recovery rate, fatigue resistance, and sag factor characterizing cushioning quality [2,4,5].

Not all VACNT forests, however, show good resilience, and some undergo significant plastic deformation after a single loading cycle [9,10]. A clear understanding of microscopic structural parameters of anisotropic CNT networks that define the balance between reversible and irreversible modes of material deformation is needed for targeted fine-tuning of the mechanical properties required for engineering applications. CNT diameter and forest

* Corresponding author.

E-mail address: lz2n@virginia.edu (L.V. Zhigilei).

density have been shown to be among the key factors that define how well a forest would recover after uniaxial compression [11]. Denser forests consisting of multi-walled nanotubes (MWCNTs) with large diameters are found to be stiffer and better able to recover after CNTs form new contacts with each other via van der Waals non-bonded interactions during compression, resulting in a better resilience in cyclic loading. The superior resilience of MWCNT forests can, in part, be attributed to the specifics of bending buckling deformation, which is characterized by appearance of localized ripples along the outer wall of a MWCNT rather than buckling kinks observed for single-walled CNTs (SWCNTs) [12–14]. This results in a strong inter-wall repulsion that acts as a restoring force for straightening of MWCNTs. Conversely, sparser forests, especially those consisting of CNTs with fewer walls, are prone to plastic deformation as the nanotubes irreversibly aggregate during compression. These differences are partially responsible for variability in the magnitude of mechanical properties (e.g., modulus of elasticity, modulus of resilience, loss coefficient) of VACNT forests reported in the literature [5,15–17]. Other important factors affecting the mechanical response of VACNT forests are the CNT-CNT contact density and morphology [18,19], CNT surface roughness [16,20], presence of defects [21,22], and strain rate [4,10,19,23]. Table 1 provides ranges of elastic properties for structurally distinct VACNT forests taken from Ref [11]. Therein, the modulus of resilience is the energy per unit mass that a material can store elastically. Mathematically, the mass specific modulus of resilience is defined as the quotient of the square of the yield strength (σ_y) over twice the elastic modulus (E) times the material density (ρ), i.e.,

$$U = \frac{\sigma_y^2}{2E\rho} \quad (1)$$

A systematic evaluation of factors affecting the mechanical properties of VACNT forests through *in situ* tests and *ex situ* analysis, however, is hampered by the difficulty of growing VACNT forests with precisely controlled structural characteristics, as well as by the large number of structural parameters, such as CNTs diameter, length, and number of walls, forest density, degree of alignment, bundle size distribution, porosity, presence of defects and cross-links, etc., which have to be controlled during the growth process. Under conditions when it is difficult, if not impossible, to grow a series of samples with the controlled variation of some of these structural characteristics while keeping other characteristics fixed, predictive and reproducible computer simulation presents an attractive approach to the exploration of the multi-dimensional space of structural parameters of CNT network materials and their effect on the mechanical properties.

Faithfully reproducing the multiscale nature of VACNT forests, from the atomic structure of CNTs to their arrangement into complex networks of interconnected bundles, has been a long-standing challenge for traditional materials modeling techniques. At the atomic scale, the molecular dynamics (MD) technique [24] has been widely used to simulate the mechanical and thermal transport properties of individual nanotubes, e.g. [25–36], and small groups of CNTs, e.g., [37–41]. Although the investigation of the properties of individual nanotubes and their interactions is a necessary step in the analysis of the behavior and properties of CNT network

materials, macroscopic properties of these materials are defined by the collective interactions of thousands of nanotubes organized into a network of bundles. The macroscopic properties, therefore, cannot be derived directly from the properties of individual nanotubes and can only be addressed in simulations performed at a length scale that encompasses a sufficiently large representative part of the network structure, which is far beyond the capabilities of the atomistic MD model.

To close the gap between the well-established atomistic description of individual nanotubes and the macroscopic properties of CNT materials that can be formulated at the continuum level in terms of constitutive relationships, a number of mesoscopic computational models [42–45] capable of simulating the collective behavior and properties of large CNT ensembles, e.g. [43,46–48], have been developed. The common features of several alternative mesoscopic models proposed for CNT materials [42–45] include the coarse-grained description of nanotubes, where nanotube segments composed of many atoms are represented by a highly reduced number of dynamic degrees of freedom. In addition, they share similar formulations of the internal parts of the mesoscopic force fields that account for the stretching and bending deformation of individual nanotubes, and are parameterized based on the results of atomistic simulations. The different models, however, adopt very distinct computational approaches for the description of the non-bonded van der Waals inter-tube interactions.

The first and most straightforward mesoscopic approach to the description of CNT-CNT interactions is based on the bead-and-spring model [42], commonly used in coarse-grained simulations of polymers [49]. In this approach, the van der Waals inter-tube interactions are modeled through spherically symmetric pair-wise interactions between mesoscopic nodes representing segments of nanotubes. Due to its simplicity, the bead-and-spring model has become a popular choice for mesoscopic modeling of CNT films [46,50–56] and VACNT arrays [57]. As discussed in Refs. [43,45,47,58], however, the pair-wise interactions between the “beads” in the bead-and-spring model introduce large artificial barriers for relative displacements of neighboring CNTs, which prevents long-range rearrangements of CNTs required for their self-assembly into continuous networks of bundles and strongly affects the structure and mechanical behavior of the CNT materials.

More recently, a “finite beam element” model [6] describing van der Waals inter-tube interactions by linear elastic bar elements added at localized “contacts” has been proposed and applied for simulation of the mechanical behavior of two-dimensional (2D) CNT forests. Although the model is capable of reproducing some of the general experimentally observed features of the stress-strain response of VACNT forests undergoing uniaxial compression, the 2D nature of the model and the description of CNT-CNT interactions by strongly localized bonds that cannot be broken in the course of the forest “growth” or compressive deformation prevent application of this model for realistic simulations of structural self-organization or mechanical properties of the CNT network materials.

More advanced descriptions of non-bonding inter-tube interactions that do not produce the artificial corrugation of the inter-tube interactions have recently been developed, namely a mesoscopic model [43,59,60] based on the distinct element method [61,62] and a model representing nanotubes as a sequence of cylindrical segments [44] interacting with each other through the tubular potential method [45]. The latter approach has been parametrized to provide a realistic description of nonlinear deformation, buckling [47] and mechanical energy dissipation in individual CNTs [63], as well as collective heat transfer in CNT materials [38,48,58,64]. This model is briefly described below, in section 2, and is used in the present paper for simulation of the uniaxial

Table 1

Typical range of mechanical properties of multi-walled VACNT forests with mass densities ranging from 0.008 to 0.2 g/cm³ [11].

Yield Strength (MPa)	Elastic modulus (MPa)	Modulus of resilience (kJ/kg)
0.02–10	1–150	0.03–3.6

compression of VACNT forests. An overview of the computational samples used in the simulations is provided in section 3 and is followed by presentation of the results of the simulations. A detailed discussion of the effect of the mesoscopic structure of the VACNT forests, compression rate, material density, and the interaction of the CNTs with the indenter on the mechanical properties and deformation behavior of the VACNT forests is provided in section 4. The results of the simulations of repetitive loading and unloading of a VACNT forest over five cycles are presented in section 5 for two different types of CNT - indenter interactions. Finally, a summary of the results is given in section 6.

2. Mesoscopic force field model for carbon nanotube materials

The mesoscopic force field model developed for realistic large-scale simulations of CNT materials is based on a coarse-grained representation of individual CNTs as chains of stretchable cylindrical segments [44]. The state of each segment is defined by positions, velocities, and internal temperatures of nodes joining the neighboring segments [44,45]. The dynamics of a system of interacting CNTs is described by solving the equations of motion of classical mechanics for the positions of all nodes [44], as well as the heat transfer equations for the internal thermal energy associated with the nodes [64,65]. The forces acting on the nodes are calculated based on a mesoscopic force field that accounts for stretching and bending deformation of individual CNTs as well as for the van der Waals interactions among the CNTs.

The potential energy defining the mesoscopic force field is expressed as $U = U_{str} + U_{bnd} + U_{T-T} + U_E$, where U_{str} and U_{bnd} correspond to the strain energies associated with stretching and bending of individual CNTs, U_{T-T} is the energy of non-bonded inter-tube interactions, and U_E is the energy of interaction between nanotubes and external bodies. The latter term is used in this work to represent the substrate as well as the indenter in simulations of uniaxial compression of VACNT arrays described throughout this paper. The harmonic parts of the stretching and bending potentials, U_{str} and U_{bnd} , are parametrized for single-walled CNTs in Ref. [44] based on the results of atomistic simulations performed with the reactive empirical bond-order (REBO) potential [66,67]. The descriptions of the transition to the anharmonic regime (nonlinear stress-strain dependence), axial buckling of CNTs under uniaxial compression, and fracture of CNTs under tension are included in U_{str} but do not play any significant role under conditions of the simulations discussed in this paper. The bending buckling is also accounted for in U_{bnd} [47] and, in contrast to the axial buckling, is found to play an important role in the compressive deformation of VACNT forests.

The inter-tube interaction term U_{T-T} is calculated based on the tubular potential method [45] that provides a non-corrugated description of relative sliding of nanotubes and accurately reproduces the van der Waals interactions between CNT segments of arbitrary lengths and orientation. The tubular potential is parametrized based on an interatomic potential for nonbonded interactions between carbon atoms used in the adaptive intermolecular REBO (AIREBO) potential [68] and is found to reproduce the predictions of the atomistic representation of the inter-tube interactions with high accuracy at a small fraction of the computational cost [45]. The mesoscopic force field does not include an explicit description of friction forces related to the relative displacement of tubes with respect to each other, as these forces are too weak to prevent room-temperature rearrangements of defect-free CNTs [69,70]. The contribution to the static friction forces originating from the changes in the inter-tube interaction area, however, is fully accounted for in the mesoscopic model.

Experimental measurements and simulations of the sliding force required to pull an inner tube from an outer one in a MWCNT [71] and the static friction between two highly crystalline double-walled CNTs and MWCNTs [45,70] reveal that the friction force is independent of the overlap area and its magnitude is comparable to that expected from the changes in the inter-tube interaction area. Atomistic simulations predict that the oscillating force originating from the atomic-scale corrugation of the inter-tube potential is more than two orders of magnitude lower than the force related to the decrease in the surface area of van der Waals interaction [71] and cannot be expected to make any significant contribution to the static friction [71,72]. As a result, the force required to pull out a nanotube from a bundle of pristine defect-free nanotubes is similar in the mesoscopic and atomistic simulations and is defined by the energy needed to create new surface [72,73]. For (10,10) CNTs considered in the present study, the CNT-CNT interaction energy is ~ 1 eV/nm [45,74], and the corresponding pullout force from a bundle is ~ 1 nN. The presence of defects, functional groups, and chemical cross-links can significantly increase the strength of the shear interactions between nanotubes [72,73], but these effects are not considered in the present study.

The model is implemented in a parallel computer code designed for large-scale simulations of CNT samples with dimensions of up to several micrometers. The initial applications of the mesoscopic model have demonstrated the ability of the model to reproduce the self-organization of CNTs into continuous networks of bundles [45,47,75] with structural characteristics similar to the ones observed experimentally, revealed the critical role the bending buckling of CNTs plays in stabilization of the network structures [47], and provided important insights into the structural dependence of the thermal transport properties of the CNT network materials [48,58,64,65]. In this work, we apply the mesoscopic model for investigation of the structure – properties relationships in VACNT forests subject to uniaxial compression. The computational samples used in the simulations are briefly described below.

3. Computational samples of VACNT forests

The generation of computational samples for mesoscopic modeling of the mechanical compression and recovery of VACNT forests is done with a recently developed method described in Ref. [75]. The method involves generation of an initial sample composed of straight nanotubes inclined with respect to the axis of the CNT forest, followed by a high-temperature annealing performed in a mesoscopic dynamic simulation which leads to the structural self-organization of CNTs into an interconnected network of CNT bundles. The choice of the maximum angle of the initial inclination of nanotubes with respect to the direction of preferred CNT alignment is found to provide a high degree of control over the structure of computational samples, thus enabling the generation of microstructurally distinct VACNT forests with tunable bundle thickness distribution and degree of nanotube alignment.

The three samples used in the present study are composed of (10,10) single-walled CNTs (SWCNTs) with a diameter of 1.357 nm [45], typical for SWCNT forests grown by chemical vapor deposition (CVD) [76–80]. The CNT areal density (*i.e.*, the number of nanotubes per unit area of the substrate) of experimental samples exhibits a large, orders of magnitude, variability [76–79] and, in order to explore the effect of density on the mechanical properties of VACNT forests, computational samples with different areal densities are considered. The first two samples, designated as FA and FB, have the same density 0.02 g/cm³ (areal density of 6.09×10^{11} CNT/cm²) but differ in their microstructure. The CNTs of FA are highly oriented and form smaller bundles as compared to FB, where CNTs are

poorly oriented but arranged into thicker bundles. The third sample, designated as FC, has a five times higher density of 0.1 g/cm³ (areal density of 3.05×10^{12} CNT/cm²). Its bundles are much thicker than those of FB, and its nanotubes are moderately inclined. For each sample, Table 2 provides details on the density, average CNT segment tilt, average bundle size, maximum bundle size, and magnitude of the Herman orientation factor (HOF) defined as $S =$

$\frac{1}{2} \left[3 \langle \cos^2 \theta \rangle - 1 \right]$, where θ is the local angle between a nanotube segment and the vertical axis and $\langle \dots \rangle$ denotes averaging over all CNT segments in a sample. The HOF quantifies the extent of the orientation of nanotubes with respect to an axis of interest, and ranges from -0.5 to 1 , where values of -0.5 , 0 , and 1 correspond to perpendicular alignment, isotropic orientation, and parallel alignment with respect to the axis, respectively. The bundle size is defined locally as the number of CNTs in a bundle cross-section, and a CNT is considered to be a part of a bundle if it is within the range of inter-tube interaction potential from any other nanotube in a bundle.

For all of the computational samples, the length of CNTs is fixed at 200 nm, periodic boundary conditions are applied in the lateral directions (parallel to the surface of the substrate), and the lateral size of the computational system is chosen to be 200×200 nm² to ensure that the mechanical behavior of the computational samples is not affected by the periodic boundary conditions. Although 200 nm is relatively short as compared to multi-micron-long samples typically used in experimental studies [2–4,81,82], we find that the stress-strain response and deformation behavior observed for VACNT forests in laboratory compression tests are reproduced in the simulations performed with the short forests. At the same time, the use of the relatively small computational systems allows us to perform a comprehensive parametric study of the dependence of deformation behavior and mechanical response of the computational VACNT forests on (1) the sample density and microstructure, (2) rate of compressive deformation, and (3) nature of the CNT - indenter interaction. Such systematic study would not be feasible for longer CNTs (and correspondingly larger lateral dimensions of the computational samples) due to the high computational cost of the simulations. Indeed, for a $200 \times 200 \times 200$ nm³ coarse-grained VACNT forest consisting of 248 nanotubes represented by approximately 25,000 dynamic elements (samples FA and FB), 1 ns of simulated time with a time step of 10 fs takes approximately 12 wall-clock hours on 16 standard compute nodes of *Comet* supercomputer at the San Diego Supercomputer Center [83] accessed through the Extreme Science and Engineering Discovery Environment (XSEDE) [84]. Given that a simulation of a uniaxial compression down to the engineering strain of 0.8 with an indenter velocity of 10 m/s takes 16 ns, running a large number of simulations for systems composed of longer tubes would put a significant strain on the available computational resources. Instead, we address the effect of CNT length on the mechanical properties of VACNT forests by performing a smaller number of simulations for

forests composed of longer CNTs. The results of these simulations will be reported elsewhere.

All simulations reported in this paper are performed at a constant temperature of 300 K, enforced by the Berendsen thermostat algorithm [85]. The stresses are calculated from the total force that the forest exerts on the indenter. The engineering strain is defined with respect to the length of the CNTs within the forest (*i.e.*, 200 nm), rather than the maximum initial forest height, which is shorter than 200 nm by less than 1%. For the convenience of representation of stress-strain dependences for VACNT forests undergoing compressive loading, we adopt a sign convention where the stress is positive in compression, and present the magnitude of the engineering strain as a positive quantity.

4. Uniaxial compression of VACNT forests

In this section, we discuss four sets of simulations of the uniaxial compression of forests FA, FB, and FC. In the first three subsections, the VACNT forests are not attached to the indenter, rather interacting with it in a purely repulsive manner. The role of the mesoscopic structure of the forest, rate of compression, and density of the material are analyzed in the first three subsections. In the last subsection, the effect of the CNT – indenter interaction is addressed based on the results of additional simulations in which the top parts of the CNTs are attached to the indenter.

4.1. Role of microstructure

In our first set of simulations, we consider forest samples FA and FB, which have the same density and differ only by their structural characteristics (*i.e.*, thickness of the bundles and CNT inclination, as seen in Table 2). Both forests are compressed at an indenter velocity of 10 m/s, corresponding to a deformation rate of 5×10^7 s⁻¹ for these 200-nm-long VACNT forests. Note that 10 m/s is a relatively fast velocity compared to the ones typically used in experiments, 1–1000 nm/s. While matching the experimental deformation rates in our simulations is not feasible due to computational limitations, the stress-strain curves obtained in the simulations are in a reasonable semi-quantitative agreement with experimental observations, suggesting that further reduction of the deformation rate is unlikely to result in major changes in the deformation mechanism. Indeed, the analysis of the dependence on the deformation behavior on the rate of compression reported in section 4.2 reveals substantial changes in the shape of stress-strain curves upon the reduction of the indenter velocity from 50 m/s to 20 m/s, and only moderate quantitative changes upon further decrease of the velocity to 10 m/s.

Snapshots from the two simulations are shown in Fig. 1, where nanotube segments adjacent to the buckling kinks are colored red. In both cases, the top parts of the nanotubes form a dense layer right below the indenter. As the indenter presses down on the forest, the nanotubes reorganize themselves to fit into the smaller volume. Ideally, the dense packing of CNTs would correspond to a horizontal, close-packed alignment of nanotubes along the substrate. However, the attachment of the nanotubes to the substrate limits the CNT rearrangement and activates multiple modes of the forest deformation. One scenario occurs when the CNTs fold over in a coordinated fashion from the base of the forest at a height where many CNTs coalesce into thick bundles. The CNTs move together when bundled, and this deformation mechanism is favored when the nanotubes belong to the thicker, less oriented bundles of FB. This deformation mode, referred to here as “folding” (the bundles fold over at their bases) is illustrated in a snapshot shown for FB compressed to 0.6 strain (Fig. 1b). Another possible response of CNT bundles to the compression is lateral deflection along its height, or

Table 2

Statistical information on structural parameters of three computational forests used in the simulations of compressive deformation reported in this paper. The density ρ , average tilt of CNT segments $\langle \theta \rangle$, average bundle size $\langle N_B \rangle$, maximum bundle size N_B^{max} , and Herman orientation factor HOF are listed for computational samples FA, FB, and FC.

Sample	ρ (g/cm ³)	$\langle \theta \rangle$	$\langle N_B \rangle$	N_B^{max}	HOF
FA	0.02	5.6°	4	10	0.96
FB	0.02	20.5°	10	36	0.73
FC	0.1	16.4°	108	315	0.83

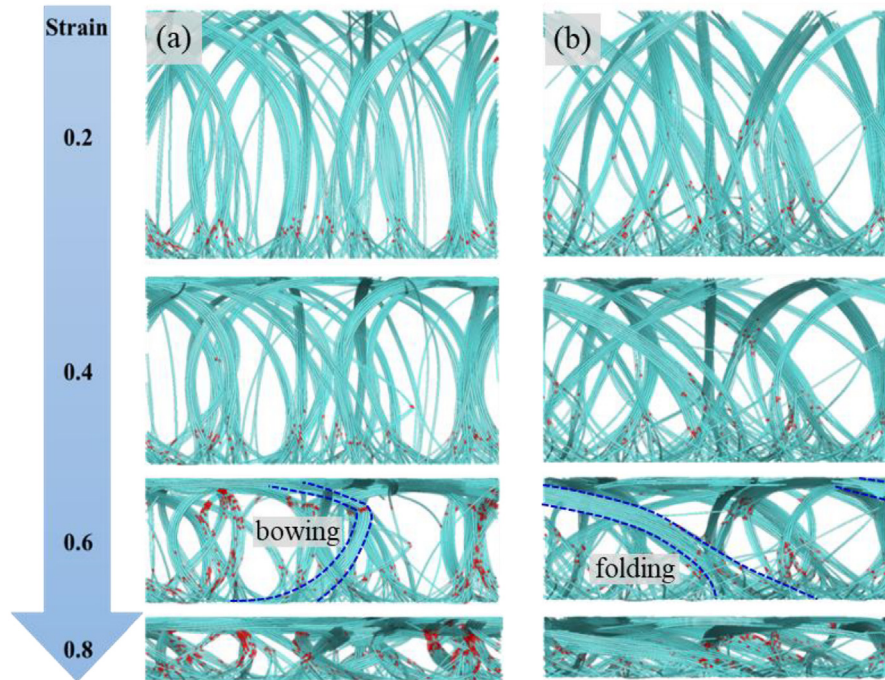


Fig. 1. Snapshots from simulations of uniaxial compression of computational samples FA (a) and FB (b) up to a maximum strain of 0.8 with an indenter velocity of 10 m/s. From top to bottom, the strain is 0.2, 0.4, 0.6, and 0.8. The CNT segments adjacent to buckling kinks are colored red. Two bundles exemplifying the bowing and folding modes of deformation are outlined by blue dashed lines in the snapshots for 0.6 strain in (a) and (b), respectively. (For interpretation of the references to color in this figure legend, the reader is referred to the Web version of this article.)

bowing outward from the initial axis of the bundle. This deformation mode, referred to herein as “bowing,” is observed for thinner, more oriented bundles, and is exemplified in a snapshot shown for FA at 0.6 strain in Fig. 1a. Although both folding and bowing deformation modes can be identified in each of the two computational samples in Fig. 1, the prevalent deformation mode is defined by structural characteristics of the samples. In particular, the smaller, more oriented bundles of FA tend to bow outward near the indenter head, while the larger, less oriented bundles of FB tend to fold near the base of the forest.

Turning our attention to the bending buckling of the nanotubes, visual analysis of Fig. 1 suggests that at a strain of 0.6 or higher CNT buckling is more prevalent in sample FA as compared to FB, and that the additional buckling appearing at later stages of compression is much more localized. In fact, FA has approximately 50% more buckling kinks than FB at a strain of 0.6, and more than double the number of buckling points of FB at a strain of 0.8. This difference can be attributed to the prevalent modes of deformation discussed above for the two samples. When bundles bow out in FA, bending stress concentrates in localized regions of the bundles, leading to the collective buckling of many nanotubes across the corresponding bundle cross-sections. A clear example of this localized collective buckling can be seen in the upper part of the bundle outlined in a snapshot shown for 0.6 strain in Fig. 1a. The folding mode of deformation characteristic of FB differs in that the bending stress resulting from compression is localized at the base of the forest, and the curvature in the upper portions of thick bundles does not reach the level required to induce bending buckling [47].

Note that neither FA nor FB exhibit the ubiquitous periodic buckling observed in experimental studies of the compression of VACNT forests [2,3,10,86] characterized by the buckling instability extending across the whole sample thickness and producing an accordion-like wavy pattern, distinct from the natural wrinkling observed during the compression of a sheet [87]. According to the

classical Euler-Bernoulli beam theory [88], the critical stress at which a column under compression deflects laterally is inversely proportional to the square of its height. Hence, the difference in the nanotube length between the computational samples and many of the repeated coordinated buckling in the computational forests [89]. Another important factor is the pristine nature of the computational samples, which do not have any defects or density variation along the vertical axis. Defects and the density gradients have been found to play a key role in the onset of coordinated buckling. In particular, the coordinated buckling often starts near the base of the forest, where the density can be lowest [4,10,81,86], and CNT diameter may be smaller [11]. Our samples do not have such types of preferential nucleation sites, and hence periodic buckling may be suppressed. Finally, the periodic boundary conditions applied in the lateral directions eliminate free surfaces on the sides of the samples and prevent the surface nucleation of the buckling instability [2,3,10].

The measurement of the stress-strain relationship is a common way to evaluate the mechanical properties of the VACNT forests. The stress-strain response of VACNT forests is usually similar to that of conventional foam-like materials and is characterized by three distinct regimes, as illustrated by Fig. 2c [86]. The initial deformation proceeds in an elastic regime characterized by a sharp increase in stress without noticeable structural changes in the material. After the initial buckling event, which can involve multiple bundles, the stress drops, giving way to the plateau regime. For VACNT forests, the plateau regime is often characterized by a corrugated, upward trending stress-strain response produced by repeated, localized, coordinated buckling occurring along the height of the forest. Buckling occurring in this regime may be either reversible or irreversible, depending on the CNT types and structural characteristics of the forest. Finally, at high strains, the forest cannot readily deform via soft bending and buckling modes, and the

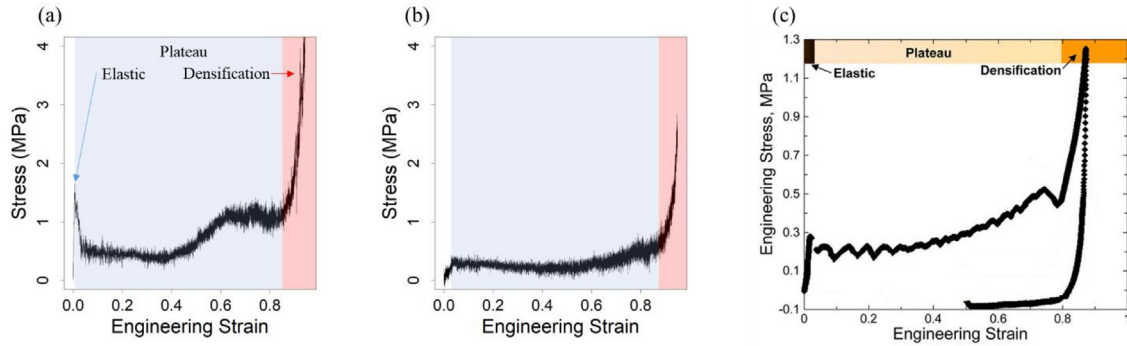


Fig. 2. Stress-strain dependences obtained in the simulations of uniaxial compression of computational samples FA (a) and FB (b) with an indenter velocity of 10 m/s, and a typical experimental stress-strain curve measured for a VACNT forest (adapted from Ref. [86]) (c). The white, blue, and red shaded regions in (a) and (b) correspond to the elastic, plateau, and densification regimes of the compressive deformation, respectively. (For interpretation of the references to color in this figure legend, the reader is referred to the Web version of this article.)

densification regime characterized by material stiffening is reached. It is important to note that the terms “elastic,” “plateau,” and “densification” do not necessarily correspond to a particular mode of deformation and are herein used to denote the stress-strain response only. For instance, the deformation occurring in what we term the elastic region is not necessarily entirely reversible due to the metastable nature of the VACNT samples. The elastic modulus and the yield strength used for characterization of the “elastic region” of stress-strain dependence are formally defined here as the slope of the initial stress increase and the maximum stress of the “elastic peak,” respectively.

The stress-strain curves obtained in the simulations performed for samples FA and FB are shown in Fig. 2a and b, respectively. Comparing these plots to Fig. 2c, we see that the three characteristic deformation regimes are clearly present. Following the unshaded elastic regime, two shaded regions identify the plateau (blue), and densification (red) regimes, which were visually discerned. Despite the much shorter length of the nanotubes and differences in the CNT types and deformation conditions, the magnitude of the stress response is in a good agreement with the experimental results, especially for the loading of sample FB. This semi-quantitative agreement suggests that the simulations capture the main deformation mechanisms that define the shape of the stress-strain curves under compressive loading. Interestingly, although the collective buckling of individual CNT bundles does not lead to the lateral propagation of the buckling instability through the computational samples (Fig. 1), the low stress plateau regime is still reproduced in the simulations, suggesting that the macro-scale periodic buckling of the forest is not the main cause of (or a necessary condition for) the flat low-stress region of the stress-strain dependence.

When drawing an analogy between the stress-strain behavior of VACNT arrays and cellular foams, it is prudent to differentiate two types of mechanical response of foam structures. Most common open and closed-cell foams exhibit bending-dominated behavior characterized by bending of the cell walls during deformation, whereas the cell walls stretch in foams exhibiting stretching-dominated deformation response [90]. From a mechanical standpoint, the bending-dominated foams are compliant but well suited for energy absorption applications due to their extended and flat plateau stress regime, while the stretching-dominated foams have a large elastic peak followed by post-yield softening, and are generally quite stiff [91]. Although the deformation mechanisms of conventional cellular foams and VACNTs are not directly comparable, there are still some interesting parallels between the stress-

strain responses of each type of material. The large spike in the elastic stress of sample FA (Fig. 2a) is similar to that of a stretch-dominated structure, whereas sample FB (Fig. 2b) behaves more like a bending-dominated foam structure. The analogy between the mechanical response of foams and VACNTs are further discussed in section 4.2, where the role of the deformation rate is considered.

In the initial elastic responses of the two samples, FA has a larger yield strength (1.66 MPa) and elastic modulus (284 MPa) as compared to FB (0.44 MPa and 8.67 MPa yield strength and elastic modulus, respectively). The reason for the more robust elastic response of sample FA is that a greater fraction of vertically-oriented nanotubes undergoes a substantial axial compression before the onset of bending and buckling. This is evidenced by a spike in the CNT stretching energy shown in Fig. 3b at the initial stage of compression, occurring at the same strains where the elastic stress reaches its peak values (Fig. 2a). The plots of the bending, axial, and inter-tube interaction energies shown in Fig. 3 for sample FA compressed at 10 m/s are qualitatively quite similar to those of sample FB (not shown), except for the absence of the pronounced axial stretching energy peak at low strains.

The initial part of the plateau regime, below 0.4 strain, is similar for forests FA and FB, although the average stress is somewhat lower for sample FB, Fig. 2a and b. At this stage of the deformation, the CNTs in both samples are able to shift themselves into low resistance configurations with relative ease. At higher strains, above 0.4, the difference between the stress-strain responses of forests FA and FB becomes apparent, as the stress exhibits a substantial increase for FA but remains fairly level for FB. This difference can be related to the distinct dominant deformation modes exhibited by the two samples. The buildup of stress in FA is attributed to the higher resistance bowing deformation, whereas the softer folding deformation mode allows for a fairly level plateau stress. At 0.6 strain, the bundles in FA are heavily bowed along their entire height (Fig. 1a). Bending becomes pronounced along the height of the entire forest rather than being mainly confined at the base of the nanotubes and near the indenter, as reflected by the proliferation of buckled segments. In the case of FB, the bending of CNTs takes place through folding at the base (Fig. 1b), and this mechanism does not fundamentally change with increased strain, resulting in a relatively level stress throughout the plateau regime. As strain increases to 0.6 for sample FA, a small dip in stress is observed as bending buckling once again becomes more localized (see Fig. 1). As a result, the bending energy concentrates in small regions along the lengths of the CNT bundles and less force is exerted on the indenter, causing the overall drop in stress.

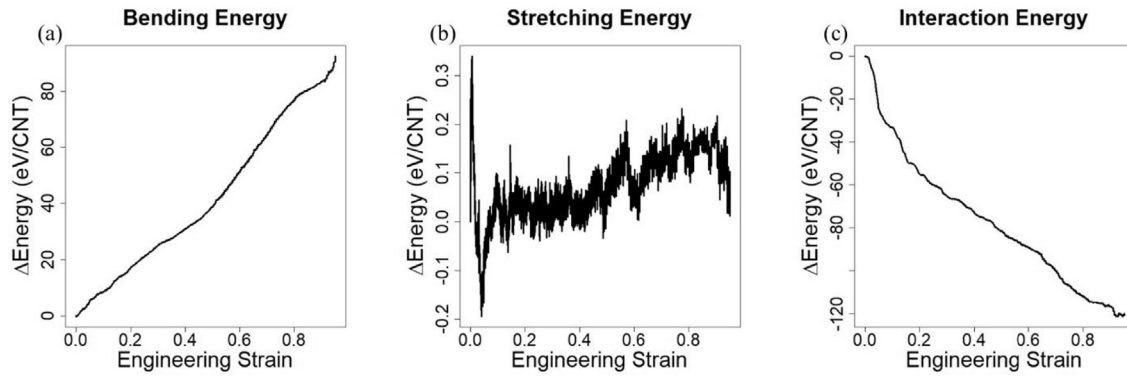


Fig. 3. Plots of the changes in (a) bending, (b) axial stretching, and (c) inter-tube interaction energies per nanotube in sample FA undergoing compression at an indenter velocity of 10 m/s.

Finally, at strains above ~ 0.85 , the densification regime begins, marked by the sharp increase in stress. During this final stage of compression, CNTs within the forest become increasingly bent and packed so that they cannot significantly rearrange themselves to reduce stress. The bending energy begins to quickly increase in the densification regime and the CNT interaction energy starts to level (Fig. 3), reflecting the increased constraints on the nanotube rearrangements.

We conclude this section by noting that the characteristic three stage stress-strain response observed experimentally for VACNT forests is reproduced for both forests FA and FB, and that their elastic stress responses fall well within the range reported for *in situ* uniaxial compressions. The two samples of the same density but different bundle thickness and orientation discussed in this section exhibit similar sequence of compressive deformation regimes, while the average plateau and densification stresses are larger in the sample with smaller, more oriented CNT bundles.

4.2. Role of compression rate

The effect of the compression rate on the mechanical response of uniaxially compressed VACNT forests has been a subject of recent investigations [4,10,19,23]. Faster compression has been linked to higher resilience, stiffness, and energy dissipation [4,10,19,92,93]. Moreover, slowly compressed forests are found to undergo permanent buckling, while forests subjected to rapid compression exhibit better recovery [4,19]. It is speculated that under conditions of fast loading the multi-walled CNTs are unable to reorganize themselves into the locally buckled structures that form, in a largely irreversible manner, when the forests are loaded more slowly. Furthermore, the stress peak in the elastic regime is observed to broaden with strain rate, and the shape of the stress undulations in the plateau regime evolves from smooth sinusoidal oscillations to much sharper sine-squared modulations at greater strain rates [10].

To better understand the effect of the compression rate on the mechanical properties of VACNT forests, we repeat the simulations presented in the previous section at higher indenter velocities of 20 and 50 m/s (deformation rates of 10^8 and 2.5×10^8 s $^{-1}$,

respectively). A snapshot showing sample FB at 0.6 strain is presented for each of the three loading rates in Fig. 4, with the corresponding stress-strain curves shown in Fig. 5. Analysis of the snapshots indicates that the increase in the loading rate shifts the dominant deformation mechanism from the “folding” to the “bowing” type (refer to Fig. 1), and that the bundles coarsen less during the shorter deformation time corresponding to the higher compression rates. The latter observation is quantified by the plots of the average bundle thicknesses shown in Fig. 6 for each of the three compression rates. The unstrained sample FA has a smaller average bundle thickness than unstrained sample FB and exhibits greater bundle coarsening with strain. However, at all but the slowest loading rate, the average bundles thickness in sample FA does not exceed the average bundle thickness of sample FB. By and large, a decrease in the compression rate leads to a more substantial coarsening of the bundles. This effect is particularly evident for forest FA, whereas the strain effect is less pronounced for sample FB (Fig. 6). The observed trends can be explained by the greater amount of time available for nanotube rearrangement into thicker bundles at slower deformation rates, as well as by a more sluggish rearrangement of the thicker bundles initially present in the unstrained sample FB.

Turning our attention to the stress-strain curves shown in Fig. 5, we notice that the general shapes of the curves are qualitatively similar for the two slower compressions, but that at 50 m/s the stress and its slope are more strongly affected by the loading rate. This trend of increasing material stiffness results from the nanotubes having insufficient time to reorganize themselves into low energy configurations as the compression rate increases. In FA, the increase in the yield strength (up to 7.21 MPa at 50 m/s) is particularly pronounced due to a more significant axial compression of the CNTs at the initial stage of the deformation (see the corresponding discussion in section 4.1). The increase in the strain rate also results in an increase in the modulus of resilience, which characterizes the maximum energy that can be absorbed in the elastic regime, see equation (1). Even at the higher strain rates, however, the values of the modulus of resilience calculated for samples FA and FB each fall within the broad range of

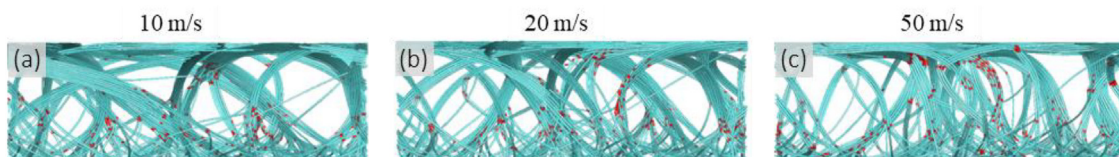


Fig. 4. Snapshots of sample FB compressed at indenter velocities of (a) 10 m/s, (b) 20 m/s, and (c) 50 m/s to an engineering strain of 0.6.

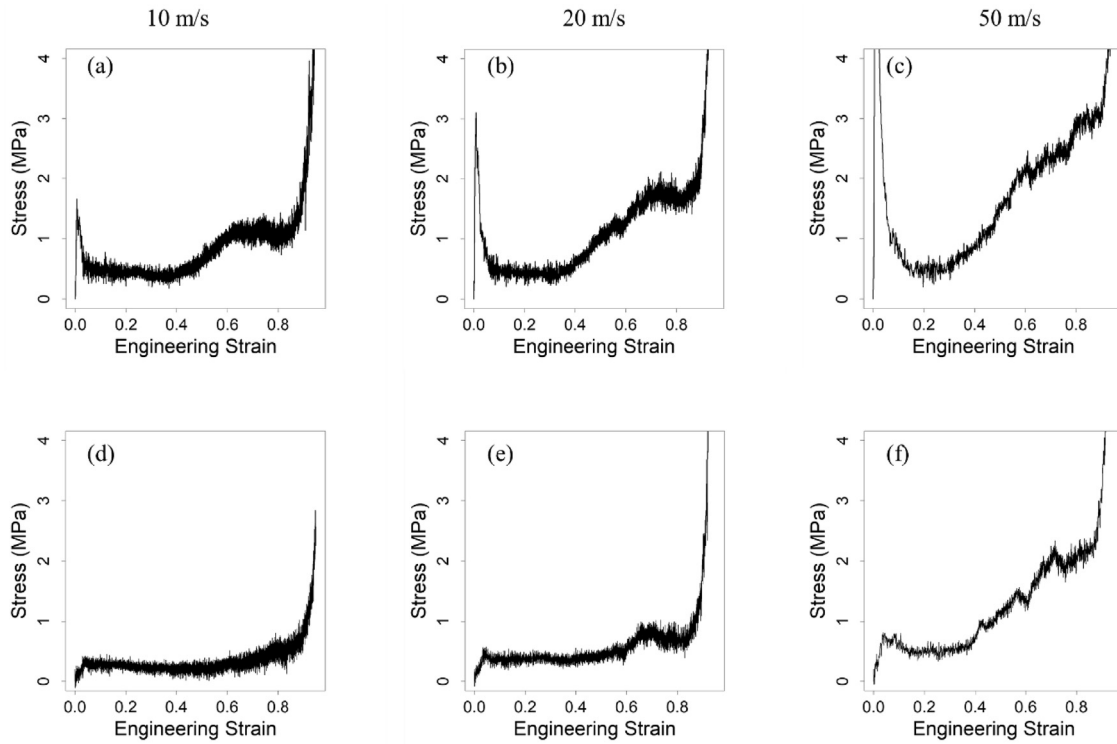


Fig. 5. Stress-strain response of samples FA (a–c) and FB (d–f) compressed at indenter velocities of 10 m/s, 20 m/s, and 50 m/s. The corresponding strain rates are 5×10^7 , 10^8 , and $2.5 \times 10^8 \text{ s}^{-1}$.

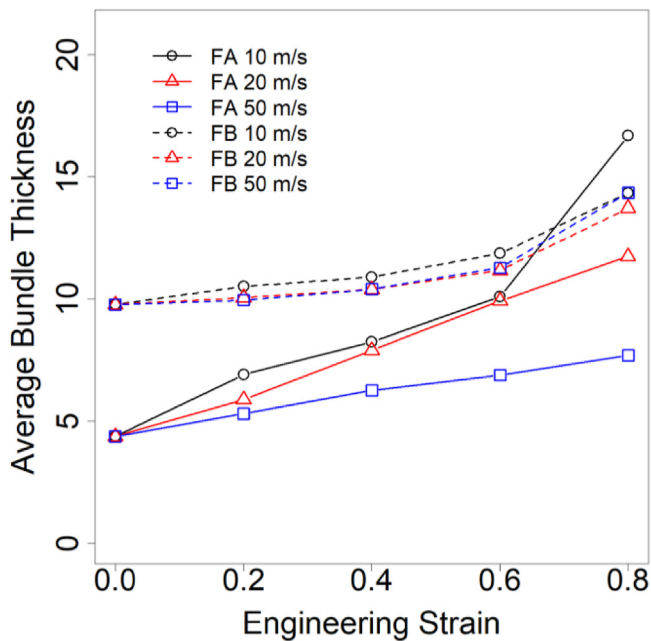


Fig. 6. The evolution of the average bundle thickness in samples FA and FB compressed with indenter velocities of 10, 20, and 50 m/s up to 0.8 engineering strain.

experimentally measured values listed in Table 1.

Continuing with the analogy to cellular foams discussed in section 4.1, the changes in the stress-strain curve with increasing strain rate observed in the simulations can be related to a shift from the bending-dominated to stretching-dominated mechanical response of foams. Not only does the elastic stress increase, but a

post-yield softening regime becomes more apparent at higher strain rates, which is also observed in *in-situ* compression experiments for CNT forests [10]. Hence, depending on the rate of compression, VACNT forests could adopt the mechanical behavior of both stretching- and bending-dominated foam structures. The broadening of the stress peak characterizing the post-yield softening arises at higher compression rates due to the reduced time that the CNTs have to reorganize themselves in a way that minimizes stress on the indenter, resulting a more gradual reduction of stress with strain.

The compression rate also affects the stress response in the plateau regime, where the plateau becomes shorter and gives way to the rising stress as the rate of the deformation increases (Fig. 5). This effect can be explained by the limitations on the deformation paths the nanotubes can take during compression at higher loading rates. Although bending buckling of the nanotubes mitigates the stress in the plateau regime, the slower compression enables the nanotubes to rearrange themselves so that bending energy is further minimized. The change in the plateau regime has important implications for energy absorption, where an ideal energy absorber is characterized by a flat and long plateau stress. The results of the simulations suggest that the loading rate may strongly influence energy absorption properties of VACNT forests.

4.3. Role of forest density

The areal density of a VACNT forest is an important parameter that directly affects the structural characteristics of the network of bundles generated during forest growth [94]. The balance between the inter-tube interaction energy and bending energy of CNTs, which defines the propensity of nanotubes to join the bundles or form interconnects between the bundles, is to a large extent defined by the areal density of the CNT array. To investigate the effect of the areal density on the structural characteristics and

mechanical properties of the CNT forests, we prepared sample FC with a density of 0.1 g/cm^3 , or five times that of samples FA and FB used in the simulations discussed in the previous two sections. The structural characteristics of sample FC can be found in Table 2. Notably, while the values of structural parameters characterizing the degree of CNT alignment, $\langle\theta\rangle$ and HOF, place sample FC in between samples FA and FB, the average and maximum bundle sizes, $\langle N_B \rangle$ and N_B^{max} , are much larger than those in the lower-density forests.

The dense forest is compressed at indenter velocities of 10, 20, and 50 m/s, with snapshots for the slowest and fastest compressions provided in Fig. 7. Like the lower-density sample with thicker bundles (sample FB), the bundles of nanotubes in sample FC tend to move in a coordinated way when compressed, with the bundles folding near the substrate. The folding of the bundles becomes less coordinated with increasing deformation rate, and a progressively larger number of bundles undergo bowing deformation. Similar to the simulations discussed in section 4.2, the contribution of the bowing deformation mode leads to higher stresses at all stages of the deformation.

The stress-strain plots obtained for sample FC and shown in Fig. 8 are qualitatively similar to those predicted in simulations for sparser forests (Figs. 2 and 5). Remarkably, many of the quantitative characteristics of the mechanical response of sample FC are also comparable to those of the samples with five times fewer CNTs. In particular, the yield strength and elastic modulus calculated for sample FC are similar to those of sample FA when the simulations performed at the same compression rate are compared. The yield strength increases by a factor of less than two from FA to FC, and the elastic modulus differs between the two forests by less than 20% for the same loading rate. These observations can be explained by a greater average inclination of CNTs in sample FC as compared to sample FA (see Table 2). The more inclined nanotubes offer less resistance to the indenter during the elastic stage of the compression, since they deform predominately by bending rather than by

axially compression, which was identified in section 4.1 as the source of the initial spike in the stress-strain curve.

The plateau stress evolves similarly between samples FA, FB, and FC at both low and high compression rates. Although the slopes and magnitudes of the plateau stresses of all three samples are comparable at 10 m/s, the slope of the stress increases more rapidly with the deformation rate for sample FC. An explanation comes from the decreased nanotube mobility in the denser forest, where CNTs tend to belong to thick bundles and are largely compelled to deform with the original parent bundles. As a result, the nanotubes cannot reorganize themselves via low energy bending and localized buckling deformations as much as they do so in sparser forests with smaller bundles.

At the final stage of the compression, a sharp increase in stress signifies the transition to the densification regime (see Fig. 8). Similar to the simulations discussed in preceding sections, the sharp rise in the magnitude of the stress in this regime does not appear to be related to CNT crowding and repulsion between the nanotubes, since the inter-tube interaction energy decreases until the end of the simulation. Instead, at the high strains, the localized bending of the thick bundles becomes extreme, resulting in a large force against the indenter (see snapshots for 0.8 strain in Fig. 7). At larger strain rates, the picture differs slightly, as the tubes start to buckle further away from the base (e.g., see snapshot for 0.6 engineering strain in Fig. 7b) and bending is distributed more uniformly along the nanotubes. In each case, the higher density and thicker bundles of FC result in a large rise in stress at lower strains compared to the sparser forest samples.

4.4. Role of CNT interaction with indenter

In all simulations discussed above, the interaction of CNTs with the indenter is assumed to be purely repulsive, presenting no barriers for lateral sliding (zero traction) of CNTs with respect to the indenter. In real compression experiments, however, there is

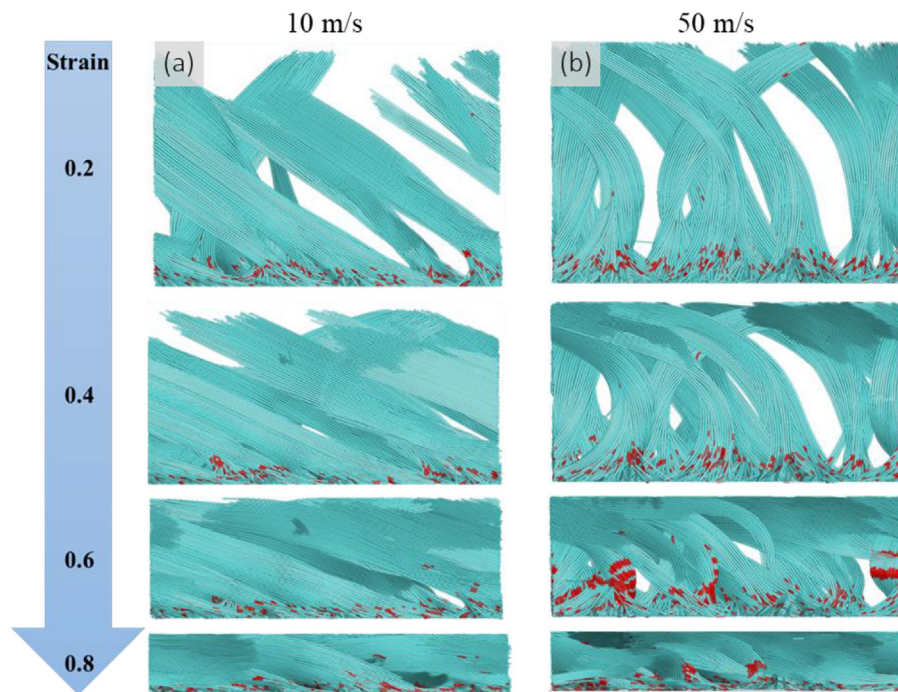


Fig. 7. Snapshots from simulations of a computational sample FC compressed at indenter velocities of (a) 10 m/s and (b) 50 m/s up to a maximum strain of 0.8. From top to bottom, the strain is 0.2, 0.4, 0.6, and 0.8. The CNT segments adjacent to buckling kinks are colored red. (For interpretation of the references to color in this figure legend, the reader is referred to the Web version of this article.)

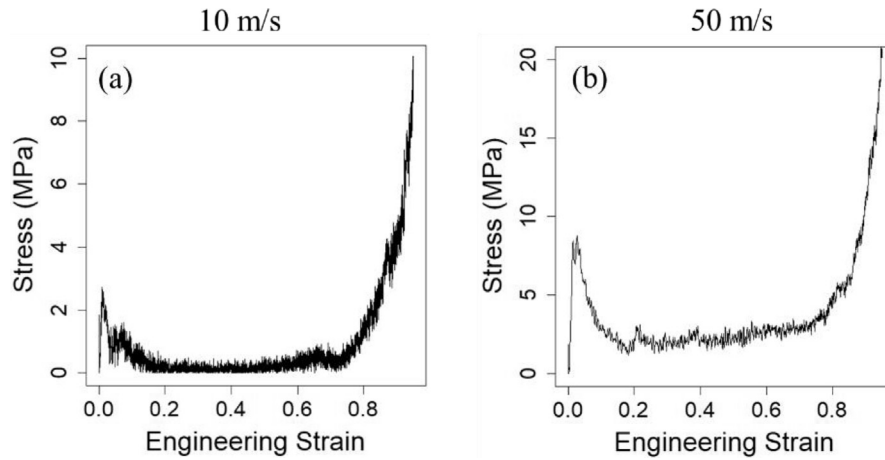


Fig. 8. Stress-strain response of sample FC compressed at indenter velocities of (a) 10 m/s and (b) 50 m/s. The corresponding deformation rates are 5×10^7 and $2.5 \times 10^8 \text{ s}^{-1}$. Note the twice larger scale of the stress axis used in (b).

generally at least some attractive interaction between the CNTs and the indenter (either non-bonding or chemical). In other words, the adhesion between the nanotubes and the indenter can manifest itself in an attractive force resisting the indenter pull off from the VACNT forest during unloading of a compressed sample [92,95]. One can also expect that the constraints on the lateral slip of the nanotubes with respect to the surface of the indenter is likely to affect the deformation behavior, particularly for short forests subjected to compression. To gain insights into the effect of the interaction between the CNTs and the indenter on the mechanical characteristics of VACNT forests undergoing compressive deformation, a series of simulations is performed for samples where the top segments of the nanotubes located within 10 nm from the indenter are permanently affixed to the indenter. These segments move together with the indenter during the compression and have no rotational freedom. The CNTs that have their top ends falling below the 10 nm cutoff distance from the indenter in the initial sample do not “stick” to it even if they get closer to the indenter during the deformation and are not affected by this boundary condition. Since the tops of many of the nanotubes are effectively “glued” to the indenter, we, shorthanded, refer to these simulations as “glue” simulations, while the simulations where the tops of the CNTs are not attracted to the indenter are referred to as “free” simulations.

The first set of glue simulations is performed for sample FA and is illustrated by snapshots shown for indenter velocities of 10 and 50 m/s in Fig. 9. Here, the nanotubes cannot deform via the folding deformation mode and, even at the slowest strain rate, the deformation proceeds through bowing of the CNT bundles. Similar to the free simulations performed for low-density samples FA and FB (see Figs. 1 and 4), bending deformation of the top parts of the CNTs leads to the formation of a dense layer adjacent to the indenters. However, since the nanotubes cannot slide along the indenters in the glue simulations, bowing of CNT bundles readily results in localized regions of collective bending buckling along the height of the bundles. This effect is particularly noticeable in Fig. 9a, where most of the CNT bundles feature well-defined regions of localized buckling (red CNT segments) at 0.6 engineering strain. In contrast, snapshots of the analogous free simulation, where CNTs interact repulsively with the indenter, show a lesser degree of buckling kink localization within the bundles (Fig. 1a). Moreover, some of the bundles in the glue simulations are observed to undergo higher-order bending producing “S” shaped, serpentine bundle shapes, such as the one outlined by dashed curves in a snapshot shown for

0.2 strain in Fig. 9b. The formation of such bending modes requires significantly higher loads and is not observed in simulations performed with the free tops of CNTs.

To make the connection between the boundary conditions applied to the nanotubes at the location of the indenter, we can turn for a qualitative guidance to the classical Euler-Bernoulli beam theory [88], which predicts the following expression for the critical load, or maximum stress, that a column can withstand without buckling:

$$P_{cr} = \frac{n^2 \pi^2 E_{bnd} I}{(KL)^2} \quad (2)$$

where E_{bnd} is the bending modulus, I is the moment of inertia about the axis of buckling, L is the length of the column, n is the column buckling mode, and K is an effective length factor defined by the boundary conditions applied at the ends of the column. The theory behind this equation has been successfully applied to the investigation of buckling [96–98] and wave propagation [99,100] in CNTs. Due to the complex structure of CNT bundles and their attachment to the substrate and the indenter, however, the classical beam theory can only be used for general qualitative guidance in the analysis of the deformation modes of bundles in VACNT forests. It is also important to distinguish the column buckling of a CNT bundle, which simply refers to the onset of its lateral deflection, from the buckling of a CNT, which is associated with an abrupt change in the shape of the nanotube cross-section and a drop in the resistance of nanotubes to bending at a critical radius of local curvature [47].

Two immediate conclusions one can draw from equation (2) are (1) the higher level of stresses needed for activation of higher order column buckling of CNT bundles ($n \geq 2$) leading to the appearance of serpentine-shaped bundles and (2) the increased likelihood that such higher levels of stresses can be generated under conditions when the upper segments of the nanotubes are fixed (the coefficient K decreases from 2 for a column with no constraints on the motion of rotation and lateral translation of the upper end to 0.5 for a column with fixed end segments of the column). Assuming that equation (2) can be applied to the description of bending of CNT bundles under compression, we can expect to see much higher stresses at the initial stage of the deformation in the glue simulations, where both ends of the CNTs are fixed ($K = 0.5$), as compared to the free simulations, where the tops of the CNTs are free to rotate and deflect laterally ($K = 2$).

Examination of the stress-strain curves from the glue

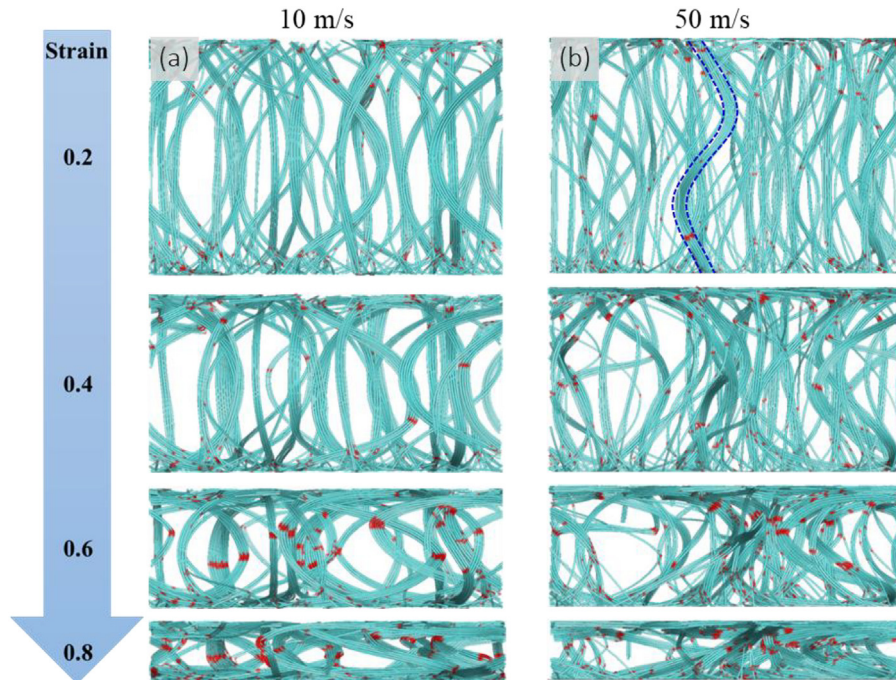


Fig. 9. Snapshots from “glue” simulations of sample FA compressed at indenter velocities of (a) 10 m/s and (b) 50 m/s up to a maximum strain of 0.8. From top to bottom, the strain is 0.2, 0.4, 0.6, and 0.8. The tops of the nanotubes are attached to the indenter, and the CNT segments adjacent to buckling kinks are colored red. A bundle exemplifying the higher-order serpentine bending of CNT bundles is outlined by blue dashed lines in the snapshots for 0.2 strain in (b). (For interpretation of the references to color in this figure legend, the reader is referred to the Web version of this article.)

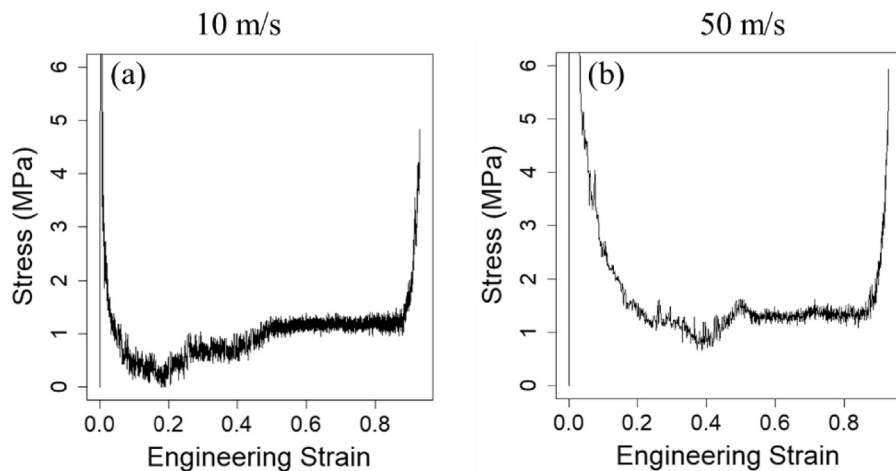


Fig. 10. Stress-strain response for sample FA compressed at indenter velocities of (a) 10 m/s and (b) 50 m/s, with the tops of the nanotubes attached to the indenter.

simulations (Fig. 10) reveals that elastic yield strength is much higher for sample FA here as compared to the case where there is no traction between the indenter and the nanotubes (Fig. 2a). The compression rate dependence of the yield strength in the glue simulations follows the upward trend, similar to that discussed in section 4.2 for simulations where the CNTs are unattached to the indenter. The elastic modulus, however, decreases from 2.4 GPa at 10 m/s to approximately 1.9 GPa at both 20 m/s and 50 m/s. The drop in the elastic modulus is in contrast with the results of the simulations with free CNT ends and can be explained by the broadening of the stress peak that corresponds to the transition from the elastic to plateau regimes of the compression with increasing deformation rate. Although the yield strength is higher, the peak of the stress shifts to higher strains with the faster

compression of the forest, thus reducing the elastic modulus.

The stress peak broadening, or post-yield softening, is also observed in the free simulations, e.g., Fig. 5, where it is attributed to the inability of nanotubes to reorganize themselves rapidly enough for minimization of stress at each step of the deformation. An additional factor in the case of the glue simulations is the appearance of the higher-order column buckling modes at high loading rates (e.g., snapshot for 0.2 strain in Fig. 9b), which support larger normal stresses applied to the indenter ($n = 2$ in equation (2)). The S shape adopted by bundles with higher order buckling obstructs the localization of bending energy, and some bundles retain their serpentine configuration throughout the compression. Indeed, comparing snapshots from the two extreme compression rates, the buckled segments are more localized at 10 m/s, compared to 50 m/s

(Fig. 9). In addition, the S shapes of the bundles obstruct bundle-bundle alignment, and therefore can also lead to greater stress on the indenter.

The association of the stress peak broadening with the relaxation of the bending deformation of CNT bundles is supported by the plots of the bending energy as a function of engineering strain for the three compression rates shown in Fig. 11. The red dashed lines cross at an arbitrary chosen point where 50% of the total increase in the bending energy during the compression has occurred. Note that the corresponding strain is the lowest for the fastest compression rate and the largest for the slowest compression rate. The rapid increase in bending energy at small strains indicates that bending of CNT bundles makes an important contribution to the initial stress peak. Therefore, the broadening of the stress peak at faster compression rates can be related to the sharper increase of the bending stress resulting in the formation of higher order column buckling of CNT bundles, followed by a gradual stress relaxation facilitated by the collective buckling of CNTs localized within bundle cross-sections.

Remarkably, the values of the plateau stresses in the glue simulations are comparable to those of the freely compressed sample FA. This observation can be rationalized by the prominent role that collective buckling plays in the glue compressions. Following the multiple localized buckling events occurring in the plateau regime, the overall picture of the deformation does not change much with further increase of the strain. Additional buckled segments form around the sites of the original buckling, and the localization of the bending deformation within the buckled segments ensure a constant level of the material resistance to the indenter within a broad range of strain extending to the densification regime.

The early onset of buckling in the glue simulations is illustrated in Fig. 12a, where the number of buckling kinks per CNT is shown as a function of strain for sample FA with free and fixed tops of the nanotubes. The nanotubes with fixed ends respond to compression immediately with widespread buckling, which is initially concentrated near the two ends of the CNTs, but later extends to the central parts of CNT bundles undergoing severe bending deformation (Fig. 9). In the simulations with free ends of the CNTs, the nanotubes slide along the indenter and do not show significant buckling until around 0.4 engineering strain. Near 0.8 engineering strain, the number of buckled kinks becomes comparable for all simulations regardless of the boundary condition at the indenter and the strain rate. Comparing the snapshots at 0.8 strain for FA compressed without attachment to the indenter at 10 m/s (Fig. 1a) and those from simulations performed at 10 and 50 m/s with the CNTs attached to the indenter (Fig. 9), we see a visually similar

picture. The sections of the compressed forests in the middle of the snapshots are not aligned parallel to the indenter and their relaxation is constrained by limited mobility of the upper and lower parts of the bundles which are incorporated into the two dense layers formed near the rigid substrate and the indenter. Further compression must result in more buckling to alleviate the stress, as the constrained CNTs cannot easily reorient themselves. The compression in the absence of alternative deformation paths leads to the onset of the densification regime signified by the rapid rise of stress, Figs. 5 and 10.

The coarsening of bundles during the compression, discussed in sections 4.1 and 4.2 and illustrated in Fig. 6, is less pronounced in the glue simulations, as can be seen from Fig. 12b. The bundles still coarsen upon compression but, for each loading velocity, the increase in the mean bundle thickness is smaller when the ends of the CNTs are attached to the indenter. The thinner bundles in the glue simulations can bend and buckle more easily, which contributes to the rapid increase in the number of buckling kinks illustrated by Fig. 12a.

To investigate the effect of forest density on the deformation behavior and mechanical properties of VACNT forests with ends of the nanotubes attached to the indenter, we perform a series of glue simulations for sample FC, which has five times higher density and much thicker bundles than sample FA discussed above (see Table 2). The snapshots from these simulations are shown in Fig. 13. Visually, the deformation of sample FC is similar to that of sample FA (Fig. 9) in that buckling is highly localized along the height of the CNT bundles, and the bundles still aggregate near the indenter. Buckling occurs at lower strains for faster compression rates, and, similarly to the sparser forest, there are multiple buckled regions along the height of some of the nanotube bundles at the compression velocity of 50 m/s.

The stress-strain response shown in Fig. 14 is, for the most part, qualitatively similar to that of the more rarified forest FA (Fig. 10), with a large elastic stress peak and a post-yield softening shoulder that is particularly pronounced at faster compression rates, followed by a plateau and densification regions. The average stress in all deformation regimes, however, is substantially higher for the denser forest FC, and scales roughly with the density of the forest. This scaling is in contrast to the weak density dependence of stress magnitude discussed in section 4.3 for simulations where the top parts of the nanotubes are free to slide with respect to the indenter.

5. Recovery of VACNT forests

One of the most attractive aspects of the mechanical behavior of

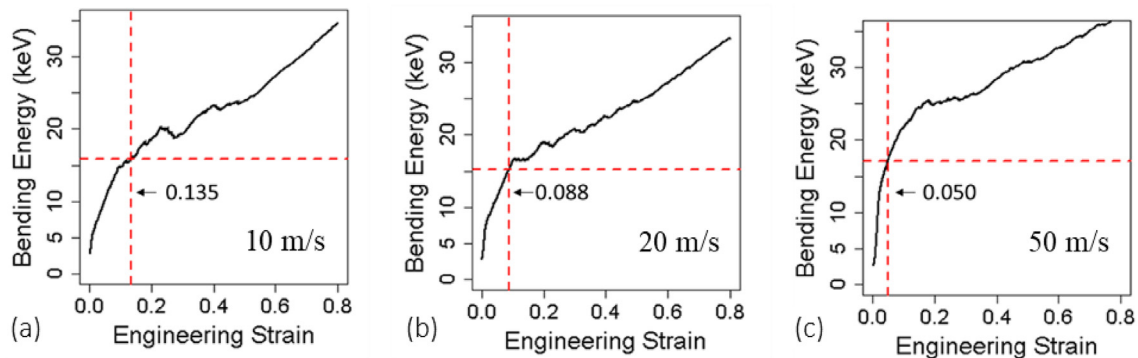


Fig. 11. Bending energy as a function of engineering strain for sample FA compressed at indenter velocities of (a) 10 m/s, (b) 20 m/s, and (c) 50 m/s, with the tops of the nanotubes attached to the indenter. The red dashed lines cross at a point where 50% of the total increase in the bending energy during the compression has occurred, with the corresponding engineering strain labeled in the figure. (For interpretation of the references to color in this figure legend, the reader is referred to the Web version of this article.)

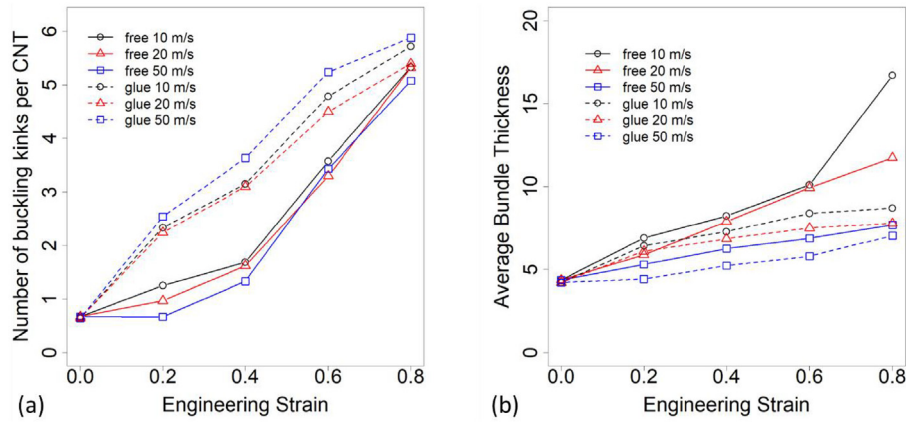


Fig. 12. The evolution of the number of buckling kinks (a) and the average bundle thickness (b) in free (solid lines) and glue (dashed lines) simulations of sample FA compressed at indenter velocities of 10, 20, and 50 m/s up to 0.8 engineering strain.

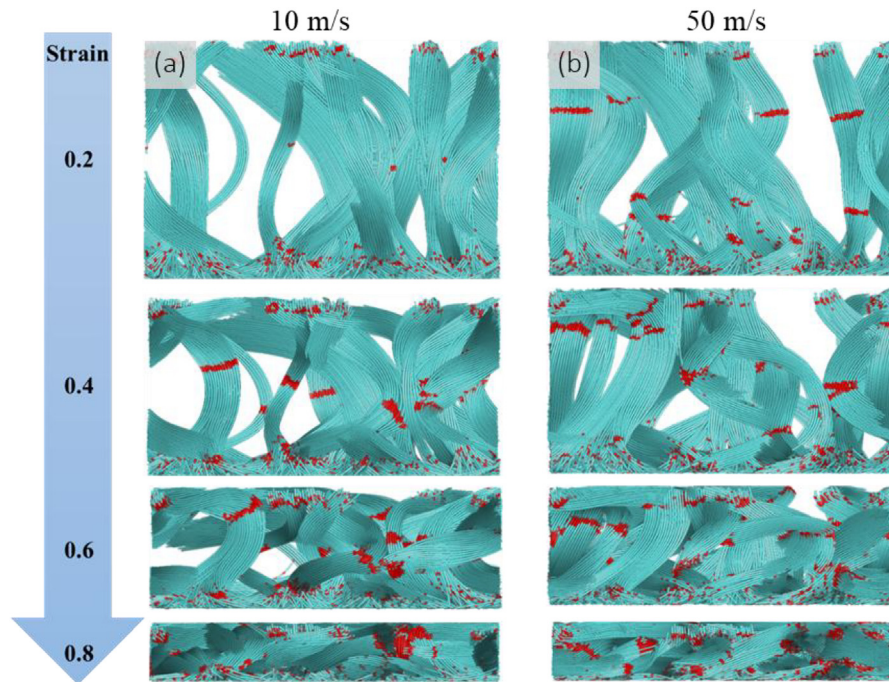


Fig. 13. Snapshots from “glue” simulations of sample FC compressed at indenter velocities of (a) 10 m/s and (b) 50 m/s up to a maximum strain of 0.8. From top to bottom, the strain is 0.2, 0.4, 0.6, and 0.8. The tops of the nanotubes are attached to the indenter, and the CNT segments adjacent to buckling kinks are colored red. (For interpretation of the references to color in this figure legend, the reader is referred to the Web version of this article.)

VACNT forests is their ability to withstand repeated loading and unloading cycles with minimal permanent deformation [2,4]. However, in some cases the CNT forest remains substantially deformed after compression [3,9,10,19]. As discussed in the introduction, factors determining the extent to which a forest will recover include the radii of CNTs, types and densities of CNT defects, strain rate, morphology, presence of inclusions, and mass density gradients along the height of the forest. As the first step in the computational analysis of the mechanisms that control the mechanical resilience of CNT forest subjected to cyclic loading, a few series of simulations where sample FA is loaded and unloaded over five cycles are performed. To explore the effect of the interaction with the indenter, both free and glue simulations of cyclic loading are performed and reported below.

5.1. Repulsive CNT – indenter interaction

In all simulations of cyclic loading, FA is subjected to five compression-recovery cycles. Each cycle consists of *compression*, where the indenter is depressed at 50 m/s, *unloading*, where the indenter is raised to the original height of 200 nm at the same velocity of 50 m/s, and *relaxation*, where the forest is allowed to recover. The relaxation stage is necessary because the forest recovery overall is significantly slower than the indenter speed of 50 m/s, and the indenter usually detaches from the forest shortly after the start of unloading. During the relaxation, most of the structural rearrangements in the forest happens within the first few nanoseconds of recovery, and by the time of 10 ns hardly any structural changes can be observed within the sample. Therefore, in the interest of reducing simulation time, we limit the cumulative

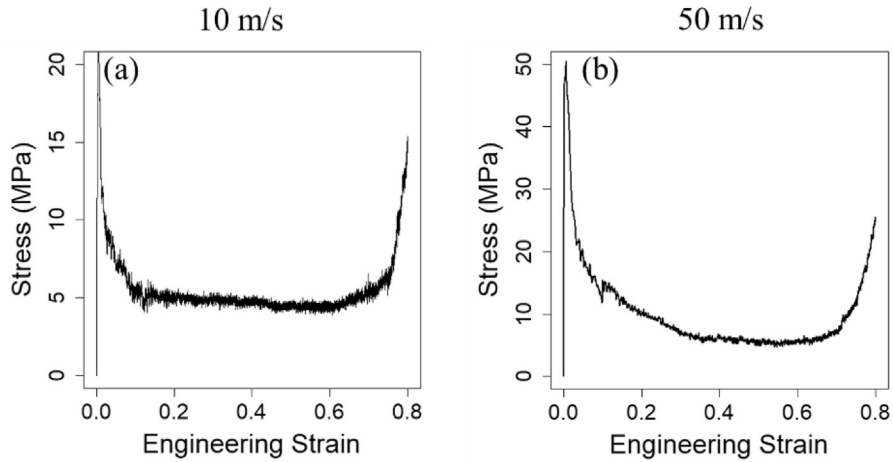


Fig. 14. Stress-strain response for sample FC compressed at indenter velocities of (a) 10 m/s and (b) 50 m/s, with the tops of the nanotubes attached to the indenter.

time of the unloading and subsequent relaxation stage to 10 ns. However, some slow structural rearrangements may still occur after 10 ns at much longer time scales.

Two simulations, with maximal compressive strains of 0.8 and 0.6, are performed for the VACNT forest where the ends of CNTs are unattached to the indenter. Snapshots from the simulations are shown for configurations formed by the end of the 1st, 3rd, and 5th loading-unloading-relaxation cycles in Fig. 15. Examining the snapshots for the forest compressed repeatedly to 0.8 strain (Fig. 15a–c), we see that recovery is limited to less than half of the original forest height, and after each cycle the maximum recovery is decreased. A dense layer of horizontally aligned CNT bundles forms at the interface with the indenter and remains stable after the indenter separates from the compressed forest during the unloading stage. The overall structure of the forest undergoes relatively small changes with the successive cycles.

The snapshots from the simulation where sample FA is compressed to a lower maximum strain of 0.6 (Fig. 15d–f) show a much

more significant recovery of the forest after the first cycle. Some of the larger bundles formed during the compression are able to return to an upright position by the end of the first cycle, Fig. 15d, while others have been entangled and do not fully recover. Furthermore, the bundle size appears on average to be much larger than that in the more strongly compressed forest in Fig. 15a. Indeed, by the end of the first cycle the average bundle thickness of sample FA compressed to 0.8 strain is less than half of that when the forest is compressed to 0.6 strain (Fig. 16). Compression results in the coarsening of bundles because the nanotubes are being forced together, but at the high loading rate ($2.5 \times 10^8 \text{ s}^{-1}$ at the indenter velocity of 50 m/s) the CNTs do not necessarily reorganize in the way that minimizes their interaction energy. Furthermore, when the forest is compressed to 0.8 strain, the nanotubes are pushed into forming a metastable network of thinner bundles. When compressed down to intermediate strains of 0.6, however, the CNTs remain sufficiently mobile to allow for substantial coarsening of bundles once the pressure from the indenter is released. Indeed,

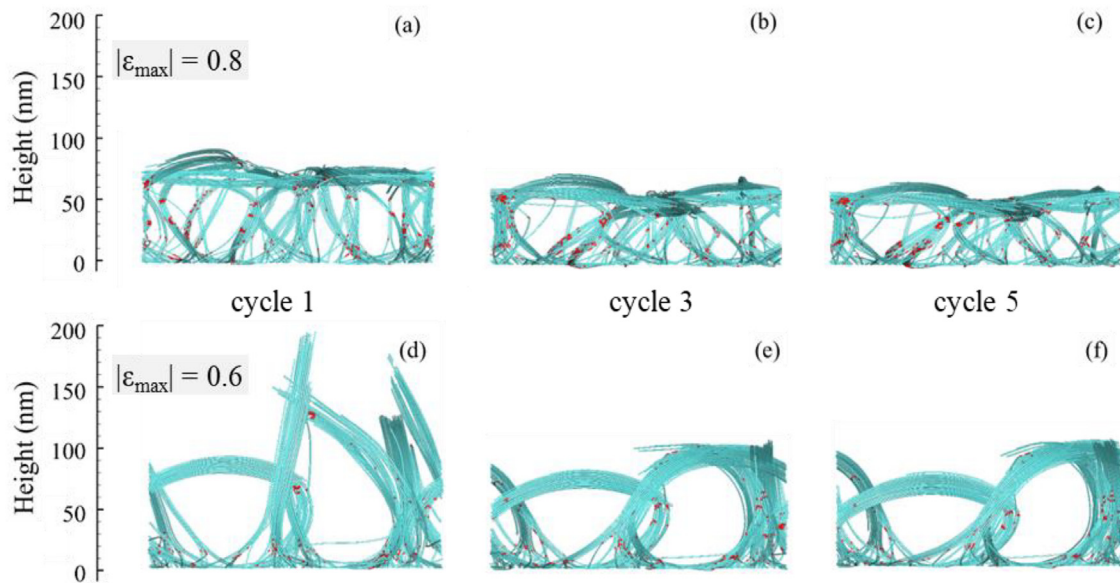


Fig. 15. Snapshots from two simulations of cyclic loading of sample FA shown at the end of cycles 1, 3, and 5. Each cycle consists of loading and unloading performed at indenter velocity of 50 m/s and followed by relaxation of the forest in the unloaded state. The loading is done up to a maximum strain of 0.8 (a–c) and 0.6 (d–f). The nanotubes are free to slide with respect to the indenter, and the CNT segments adjacent to buckling kinks are colored red. (For interpretation of the references to color in this figure legend, the reader is referred to the Web version of this article.)

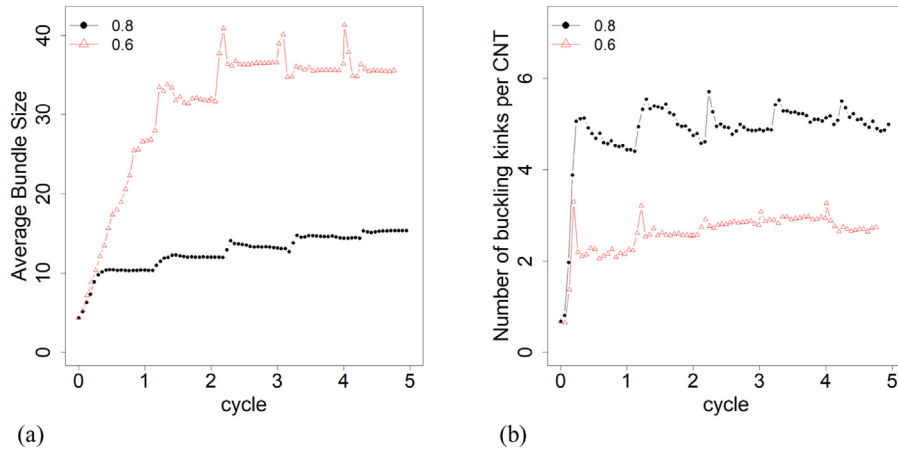


Fig. 16. The evolution of the average bundle size (a) and number of buckling kinks (b) in two simulations of cyclic loading of sample FA. Each of the five consecutive cycles consists of loading and unloading performed at indenter velocity of 50 m/s and followed by relaxation of the forest in the unloaded state. The loading is done up to a maximum strain of 0.8 (black line and dots) and 0.6 (red lines and triangles). The simulations are performed for nanotubes that are free to slide with respect to the indenter. (For interpretation of the references to color in this figure legend, the reader is referred to the Web version of this article.)

examination of Fig. 16 reveals that the largest increase in bundle size for the forest compressed to 0.6 strain comes during the relaxation stage of the first cycle, *i.e.*, between cycle 0.5 and 1.0.

The structural changes in the VACNT forests undergoing cyclic loading are reflected by the number of buckling kinks plotted for each simulation in Fig. 16b. In general, the number of buckling kinks increases when the samples are compressed and decreases when the indenter is removed. The increase is particularly large at the loading stage of the first cycle, and becomes less pronounced in the following cycles. When the compression is up to a strain of 0.8, the substantial increase and partial recession in the number of buckling kinks is observed for the first three cycles, but the variation in the number of buckling kinks becomes muted during the last two cycles. Some of the CNT segments unbuckle as the forest recovers, but the degree of recovery, as seen in Fig. 15, decreases with each cycle, and the bending deformation becomes increasingly localized within the existing buckled regions of the CNT bundles. Interestingly, when FA is compressed to 0.6 strain only, the increase in the number of buckling kinks during compression is only faintly observable beyond the first two loading cycles. The high energy cost associated with collective buckling of thick CNT bundles formed in this simulation during the first loading cycle makes the deflection of the bundles by the indenter the favored deformation mode at the intermediate strains.

The ability of some of the VACNT forests to withstand multiple loading cycles with minimal plastic/irreversible deformation is of particular practical interest and can be quantified by the dimensionless loss coefficient,

$$\eta = \frac{\Delta U_i}{2\pi U_r}, \quad (3)$$

where $\Delta U_i = \oint \sigma d\varepsilon$ is the mechanical energy dissipated in the i^{th} cycle of loading and unloading, ε is the strain, and $U_r = \int_{\varepsilon_{\min}^i}^{\varepsilon_{\max}^i} \sigma d\varepsilon$ is the energy stored in the material after one compression. Here, ε_{\min}^i and ε_{\max}^i are denoting the minimum and maximum strains during a cycle, where ε_{\min}^i is not necessarily equal to zero. The quantity U_r can refer to the area under the stress-strain curve for the first compression or, alternatively, to the area for the current i^{th} loading cycle [101]. Graphically, the mechanical hysteresis loops for the

loading and unloading of sample FA up to 0.6 and 0.8 maximum strains are shown in Fig. 17b and c, respectively. The area inside each loop represents the value of ΔU_i obtained for each cycle i by subtracting the area under the unloading curve from the one under the loading curve. Visually, this area shrinks with each successive cycle. Setting U_r equal to the area under the first loading curve, we see that the loss coefficient is decreasing with each successive cycle, Fig. 17a. This decrease of the loss coefficients reflects an increasing permanent deformation of the forest sample subjected to cyclic loading.

The loss coefficient of the first cycle is almost identical in the two simulations, despite the much more substantial recovery of sample FA compressed to 0.6 strain. The reason is that there is almost no stress from the forest on the indenter at the unloading stage of the cycle, as the indenter is raised with a velocity of 50 m/s, which is too fast for the top part of the forest to follow. As a result, the stress drops down to zero shortly after the start of the unloading (Fig. 17b), and $\frac{\Delta U_i}{U_r} \approx 1$ in both simulations. The loss coefficients calculated for the subsequent cycles using the values of U_r evaluated for the first cycles are decreasing in both simulations due to the accumulation of irreversible structural changes, which result in the decreasing extent of the recovery. Moreover, in the case of the lower maximum strain of 0.6, the diminishing peak stress leads to a steeper decrease of the loss coefficient during the cyclic loading relative to the simulation with maximum strain of 0.8, where the peak stress remains fairly constant, Fig. 17b. The persistent peak stress in the latter case can be related to a resilient spring-like structure generated below the topmost, dense layer after the first loading-unloading cycle, Fig. 15a. The subsequent loading cycles only marginally affect the structure of the lower layer of the forest and the corresponding values of the peak stress.

Overall, the trend in the decay and the magnitudes of the loss coefficient are in a good agreement with experimental data [4,19], even though the parameters of the simulated forests (*i.e.* CNT diameters, forest height, lack of defects or density gradients) are rather different from most of the laboratory grown samples. Similar to the experiments, we observe the sharp drop in the loss coefficient on the second cycle followed by a gradual decline for subsequent cycles.

5.2. CNTs attached to indenter

Additional insights into the resilience of VACNT forests can be

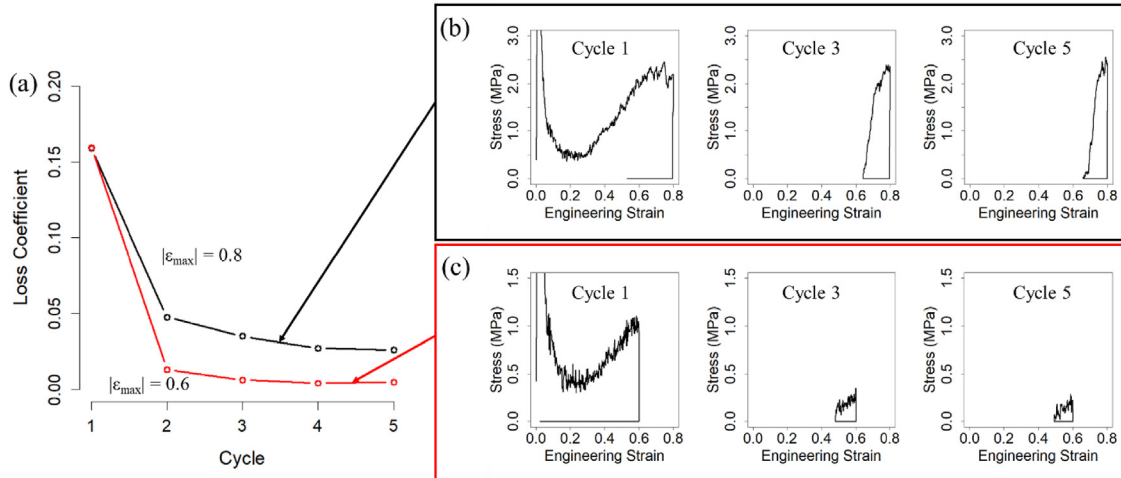


Fig. 17. Loss coefficient evaluated in simulations of cyclic loading of sample FA done up to a maximum strain of 0.8 and 0.6 (a) and the corresponding stress-strain curves shown for cycles 1, 3, and 5 (b,c). The simulations are performed for nanotubes that are free to slide with respect to the indenter.

gleaned from simulations of cyclic loading in which the tops of the CNTs are attached to the indenter (see section 4.4). Similar to the simulations discussed in the previous section, the simulations discussed below are performed for sample FA subjected to five consecutive loading – unloading cycles. However, no relaxation phase is included since the CNTs are fixed to the indenter. The effect of the loading rate is investigated by comparing the results obtained with two velocities of the indenter at the compression and recovery stages of each cycle, 10 and 50 m/s. The forest is compressed to a maximum strain of 0.8 in both simulations. In the initial test simulations, the forest samples were recovered to their initial heights, *i.e.*, back to zero engineering strain. Due to the reorganization of CNTs upon the initial compression, however, large tensile stresses arise when the height of the forest is recovered past 0.2 strain. Therefore, to avoid the large tensile stresses, we limited the recovery of the sample to 0.2 strain with respect to its

original height in all simulations discussed in this section. Starting from the second loading–unloading cycle, the duration of one cycle in these simulations is 24 and 4.8 ns for the indenter velocities of 10 and 50 m/s, respectively.

Snapshots from the simulations are shown for configurations generated by the end of 1st, 3rd, and 5th loading cycles in Fig. 18. We can see that the overall structure changes only marginally after the first loading cycle, and the primary visually apparent difference between the consecutive snapshots is a gradual coarsening of the bundles. The coarsening of the bundles is quantified in Fig. 19a, where the average thickness of the bundles is characterized by periodic variation of the bundle thickness in each loading and unloading cycle, indicating the temporary formation and splitting of bundles. However, average bundle thickness increases over the course of five cycles.

An interesting observation is that the average bundle thickness

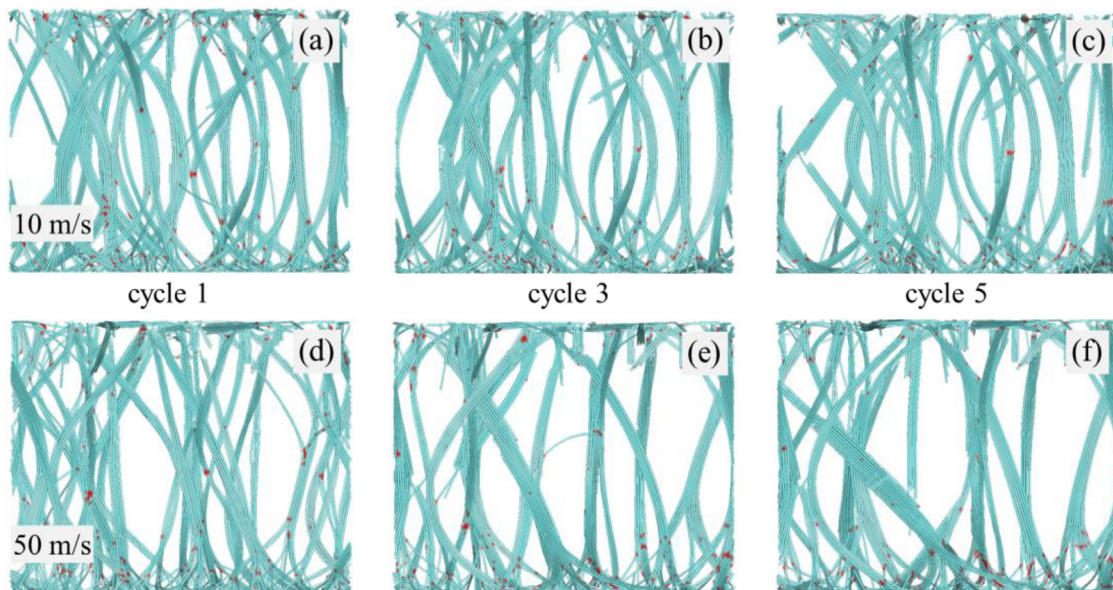


Fig. 18. Snapshots from two simulations of a cyclic loading of sample FA performed with indenter velocities of 10 m/s (a–c) and 50 m/s (d–f). The unloading is done down to a strain of 0.2 with respect to the original height of the forest. The nanotubes are attached to the indenter, and the snapshots are shown at the ends of cycles 1, 3, and 5. The CNT segments adjacent to buckling kinks are colored red. (For interpretation of the references to color in this figure legend, the reader is referred to the Web version of this article.)

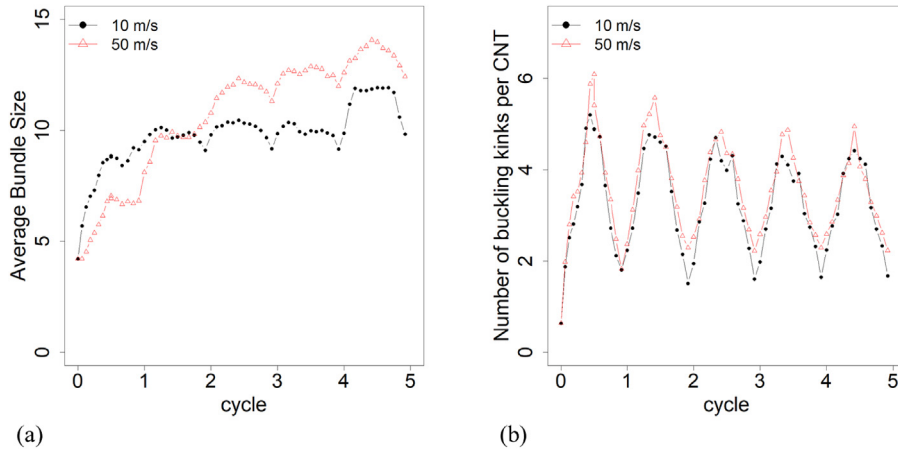


Fig. 19. The evolution of the average bundle size (a) and number of buckling kinks (b) in two simulations of cyclic loading of sample FA performed with indenter velocities of 10 m/s (black lines and dots) and 50 m/s (red lines and triangles). The nanotubes are attached to the indenter, and the unloading is done down to a strain of 0.2 with respect to the original height of the forest. (For interpretation of the references to color in this figure legend, the reader is referred to the Web version of this article.)

in the sample loaded at a higher deformation rate surpasses that in the slowly loaded sample by the end of the 2nd cycle, Fig. 19a. Although we rationalized in sections 4.2 and 4.4 that, due to extra time available for the nanotube reorganization, the CNT bundles coarsen more readily when compressed slowly, the picture becomes more complicated when the forest is attached to the indenter and undergoes multiple loading-unloading cycles. At the slower loading rate, thick and stable bundles form during the first compression, and pronounced coarsening does not occur in subsequent cycles. However, at 50 m/s, the initial compression produces relatively thin bundles, which with additional cycles continue to coarsen into even thicker bundles than those produced with the 10 m/s loading rate.

The numbers of buckling kinks shown for the two rates of deformation in Fig. 19b exhibit a nearly linear increase and decrease during the loading and unloading of the sample. The peak number of buckling kinks gradually decreases for the first several loading cycles, and the bending energy (not shown) follows a qualitatively similar trend. These decreases in the peak bending energy and the maximum number of buckling kinks reflect the increased localization of bending deformation with successive cycles. Rearrangement of nanotubes into thicker bundles reduces the number of

isolated buckling events in individual CNTs and thin bundles and makes the coordinated localized buckling of bundles the dominant mode of the bending deformation.

The loss coefficients and mechanical hysteresis cycles for the two simulations are shown in Fig. 20. The stress-strain cycles are different from the ones observed in the simulations where the CNTs interact repulsively with the indenter (Fig. 17) in that the stress does not drop to zero with the start of the recovery stage of the cyclic loading. Rather, the stress gradually decreases upon unloading and, due to the entanglement and coarsening of CNT bundles, can become tensile (*i.e.*, negative within the convention adopted in this paper) by the end of the unloading, when the forest pulls back on the rising indenter.

The loss coefficient, calculated for both loading rates using equation (3) and plotted in Fig. 20a, exhibits the same general trend that was observed for the simulations where the CNTs are not attached to the indenter, Fig. 17a. The slower deformation rate yields a larger loss coefficient since the area under the stress curve during the initial loading, U_r , is similar in magnitude to those in the subsequent loading cycles. For the faster loading rate, the difference between the level of stress realized during the initial loading and stresses observed in the subsequent cycles is greater due to the

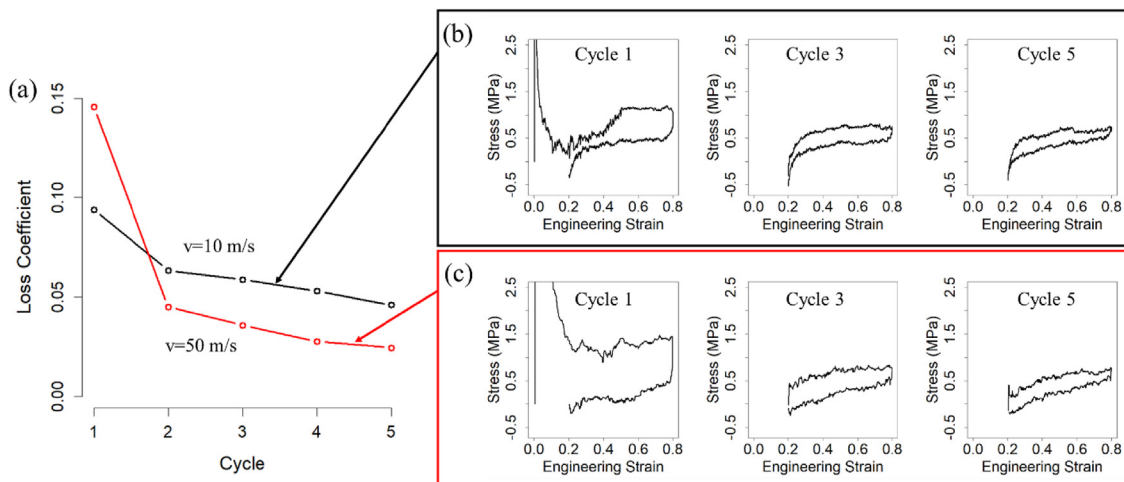


Fig. 20. Loss coefficient evaluated in simulations of cyclic loading of sample FA performed with indenter velocities of 10 m/s and 50 m/s (a) and corresponding stress-strain curves shown for cycles 1, 3, and 5 (b,c). The nanotubes are attached to the indenter, and the unloading is done down to a strain of 0.2 with respect to the original height of the forest.

more extensive structural reorganization of the nanotubes, thus resulting in smaller values of the loss coefficient. The trend of the reduction of loss coefficient in the course of the cyclic loading observed in the simulations is in a good qualitative and quantitative agreement with experimental results obtained for longer MWCNT forests [4,19].

6. Summary

The mechanical response of short VACNT forests to the uniaxial compression is systematically investigated in mesoscopic dynamic simulations performed for computational samples with different density and microstructure (bundle size distribution and degree of nanotube alignment). The effects of the loading rate and the interaction of CNTs with the indenter on the mechanical properties and deformation behavior of VACNT forests are studied and related to experimental observations. The mechanisms that control the mechanical resilience of CNT forests are also explored in simulations of cyclic loading of the computational samples.

The simulations provide first insights into structural changes in the networks of interconnected CNT bundles undergoing mechanical deformation and reveal the key elementary processes responsible for the reversible and irreversible modes of the mechanical deformation. Remarkably, the three-stage stress-strain dependence (an elastic peak followed by an extended plateau region and a sharp rise of stress in the densification regime) commonly measured for VACNT forests ranging up to millimeters in height is reproduced in the simulations performed for relatively short forests composed of 200-nm-long nanotubes. Moreover, the mechanical properties derived from the stress-strain curves (e.g. elastic modulus, yield strength, modulus of resilience) fall within the ranges reported in experimental studies.

The connections between the structural characteristics of the computational forests and their mechanical response to the uniaxial loading are investigated. The characteristic features of the stress-strain dependence are related to the thickness of CNT bundles and the degree of their alignment along the vertical axes of the forests. In particular, the mechanical behavior of short CNT forests is found to be largely defined by the competition between two distinct mechanisms of CNT bundle deformation: (i) folding of bundles at their bases, prevalent in samples with large bundle inclination with respect to the vertical axis and (ii) bowing of bundles followed by collective buckling of CNTs localized within bundle cross-sections, characteristic of vertically aligned bundles with small initial inclinations. The loading rate and density of the forest are found to have a substantial effect on the parameters of the stress-strain dependence and the deformation mechanisms. Furthermore, the effect of the interaction of CNTs with the indenter is examined, and the deformation of forests with CNT ends attached to the indenter is determined to proceed primarily through localized bending and buckling of bundles, resulting in a relatively level plateau region of stress extending past 0.8 strain.

Additionally, several sets of simulations of VACNT arrays undergoing five loading–unloading cycles are performed to examine the effect of the strain rate and maximum compressive strain on the mechanical resilience of the nanotube forests. The variation of the magnitude of the loss coefficient over successive loading–unloading cycles predicted in the simulations is in a good agreement with the results of experimental measurements. The maximum compressive strain is found to have a strong impact on the structural rearrangement of the CNTs, thus affecting the forest recovery and the peak stress when the CNTs interact repulsively with the indenter. In the simulations where the CNTs are attached to the indenter, the rate of compression is found to affect the bundling of CNTs, with a faster rate ultimately producing thicker bundles and, therefore,

lower loss coefficient as compared to slower compression rates.

Overall, the complexity of the deformation behavior of VACNT arrays, defined by the interplay of different modes of collective bundle deformation, and the high sensitivity of the mechanical response to the forest morphology, density, deformation rate, and interaction with the indenter suggest a broad range of opportunities for tuning the mechanical properties of nanotube forests to the needs of practical applications.

Acknowledgments

Financial support for this work is provided by the National Aeronautics and Space Administration (NASA) through an Early Stage Innovations grant from NASA's Space Technology Research Grants Program (NNX16AD99G). Computational support is provided by the National Science Foundation (NSF) through the Extreme Science and Engineering Discovery Environment (Project CTS160026) and by NASA's Advanced Supercomputing (NAS) Division.

References

- [1] E.G. Rakov, *Materials made of carbon nanotubes. The carbon nanotube forest*, *Russ. Chem. Rev.* 82 (2013) 538–566.
- [2] A. Cao, P.L. Dickrell, W.G. Sawyer, M.N. Ghasemi-Nejhad, P.M. Ajayan, *Supercompressible foamlike carbon nanotube films*, *Science* 310 (2005) 1307–1310.
- [3] A.A. Zbib, S.D. Mesarovic, E.T. Lilleodden, D. McClain, J. Jiao, D.F. Bahr, *The coordinated buckling of carbon nanotube turfs under uniform compression*, *Nanotechnology* 19 (2008) 175704.
- [4] S. Pathak, E.J. Lim, P.P. Abadi, S. Graham, B.A. Cola, J.R. Greer, *Higher recovery and better energy dissipation at faster strain rates in carbon nanotube bundles: an in-situ study*, *ACS Nano* 6 (2012) 2189–2197.
- [5] J. Suhr, P. Victor, L. Ci, S. Sreekala, X. Zhang, O. Nalamasu, P.M. Ajayan, *Fatigue resistance of aligned carbon nanotube arrays under cyclic compression*, *Nat. Nanotechnol.* 2 (2007) 417–421.
- [6] M.R. Maschmann, *Integrated simulation of active carbon nanotube forest growth and mechanical compression*, *Carbon* 86 (2015) 26–37.
- [7] F.A. Hill, T.F. Havel, A.J. Hart, C. Livermore, *Storing elastic energy in carbon nanotubes*, *J. Micromech. Microeng.* 19 (2009) 094015.
- [8] F.A. Hill, T.F. Havel, A.J. Hart, C. Livermore, *Characterizing the failure processes that limit the storage of energy in carbon nanotube springs under tension*, *J. Micromech. Microeng.* 20 (2010) 104012.
- [9] Q. Zhang, Y.C. Lu, F. Du, L. Dai, J. Baur, D.C. Foster, *Viscoelastic creep of vertically aligned carbon nanotubes*, *J. Phys. D Appl. Phys.* 43 (2010) 315401.
- [10] S.B. Hutchens, L.J. Hall, J.R. Greer, *In situ mechanical testing reveals periodic buckle nucleation and propagation in carbon nanotube bundles*, *Adv. Funct. Mater.* 20 (2010) 2338–2346.
- [11] O. Yaglioglu, A.Y. Cao, A.J. Hart, R. Martens, A.H. Slocum, *Wide range control of microstructure and mechanical properties of carbon nanotube forests: a comparison between fixed and floating catalyst CVD techniques*, *Adv. Funct. Mater.* 22 (2012) 5028–5037.
- [12] I. Nikiforov, D.B. Zhang, R.D. James, T. Dumitrică, *Wavelike rippling in multiwalled carbon nanotubes under pure bending*, *Appl. Phys. Lett.* 96 (2010) 123107.
- [13] C.G. Wang, Y.P. Liu, J. Al-Ghalith, T. Dumitrică, M.K. Wadde, H.F. Tan, *Buckling behavior of carbon nanotubes under bending: from ripple to kink*, *Carbon* 102 (2016) 224–235.
- [14] H. Jackman, P. Krakhmalev, K. Svensson, *Mechanical behavior of carbon nanotubes in the rippled and buckled phase*, *J. Appl. Phys.* 117 (2015) 084318.
- [15] T. Tong, Y. Zhao, L. Delzeit, A. Kashani, M. Meyyappan, A. Majumdar, *Height independent compressive modulus of vertically aligned carbon nanotube arrays*, *Nano Lett.* 8 (2008) 511–515.
- [16] P.D. Bradford, X. Wang, H.B. Zhao, Y.T. Zhu, *Tuning the compressive mechanical properties of carbon nanotube foam*, *Carbon* 49 (2011) 2834–2841.
- [17] C.P. Deck, J. Flowers, G.S.B. McKee, K. Vecchio, *Mechanical behavior of ultralong multiwalled carbon nanotube mats*, *J. Appl. Phys.* 101 (2007) 023512.
- [18] C.M. McCarter, R.F. Richards, S.D. Mesarovic, C.D. Richards, D.F. Bahr, D. McClain, J. Jiao, *Mechanical compliance of photolithographically defined vertically aligned carbon nanotube turf*, *J. Mater. Sci.* 41 (2006) 7872–7878.
- [19] S. Pathak, J.R. Rane, C. Daraio, *Effect of morphology on the strain recovery of vertically aligned carbon nanotube arrays: an in situ study*, *Carbon* 63 (2013) 303–316.
- [20] J.R. Rane, A. Misra, C. Daraio, *Tailoring the microstructure and mechanical properties of arrays of aligned multiwall carbon nanotubes by utilizing different hydrogen concentrations during synthesis*, *Carbon* 49 (2011)

- 3631–3638.
- [21] E.F. Antunes, A.O. Lobo, E.J. Corat, V.J. Trava-Airoldi, A.A. Martin, C. Verissimo, Comparative study of first- and second-order Raman spectra of MW/CNT at visible and infrared laser excitation, *Carbon* 44 (2006) 2202–2211.
- [22] E.F. Antunes, A.O. Lobo, E.J. Corat, V.J. Trava-Airoldi, Influence of diameter in the Raman spectra of aligned multi-walled carbon nanotubes, *Carbon* 45 (2007) 913–921.
- [23] J.R. Raney, F. Fraternali, C. Daraio, Rate-independent dissipation and loading direction effects in compressed carbon nanotube arrays, *Nanotechnology* 24 (2013) 255707.
- [24] M.P. Allen, D.J. Tildesley, *Computer Simulation of Liquids*, 2 ed., Oxford University Press, New York, 2017.
- [25] B.I. Yakobson, C.J. Brabec, J. Bernholc, Nanomechanics of carbon tubes: instabilities beyond linear response, *Phys. Rev. Lett.* 76 (1996) 2511–2514.
- [26] S. Iijima, C. Brabec, A. Maiti, J. Bernholc, Structural flexibility of carbon nanotubes, *J. Chem. Phys.* 104 (1996) 2089–2092.
- [27] T. Xiao, K. Liao, Nonlinear elastic properties of carbon nanotubes subjected to large axial deformations, *Phys. Rev. B* 66 (2002) 153407.
- [28] T. Belytschko, S.P. Xiao, G.C. Schatz, R.S. Ruoff, Atomistic simulations of nanotube fracture, *Phys. Rev. B* 65 (2002) 235430.
- [29] S.L. Mielke, D. Troya, S. Zhang, J.L. Li, S.P. Xiao, R. Car, R.S. Ruoff, G.C. Schatz, T. Belytschko, The role of vacancy defects and holes in the fracture of carbon nanotubes, *Chem. Phys. Lett.* 390 (2004) 413–420.
- [30] K.M. Liew, X.Q. He, C.H. Wong, On the study of elastic and plastic properties of multi-walled carbon nanotubes under axial tension using molecular dynamics simulation, *Acta Mater.* 52 (2004) 2521–2527.
- [31] C.M. Wang, Y.Y. Zhang, Y. Xiang, J.N. Reddy, Recent studies on buckling of carbon nanotubes, *Appl. Mech. Rev.* 63 (2010) 030804.
- [32] J. Park, M.F.P. Bifano, V. Prakash, Sensitivity of thermal conductivity of carbon nanotubes to defect concentrations and heat-treatment, *J. Appl. Phys.* 113 (2013) 034312.
- [33] S. Berber, Y.K. Kwon, D. Tomanek, Unusually high thermal conductivity of carbon nanotubes, *Phys. Rev. Lett.* 84 (2000) 4613–4616.
- [34] R.N. Salaway, L.V. Zhigilei, Molecular dynamics simulations of thermal conductivity of carbon nanotubes: resolving the effects of computational parameters, *Int. J. Heat Mass Tran.* 70 (2014) 954–964.
- [35] Z.P. Xu, M.J. Buehler, Strain controlled thermotability of single-walled carbon nanotubes, *Nanotechnology* 20 (2009) 185701.
- [36] C.L. Ren, W. Zhang, Z.J. Xu, Z.Y. Zhu, P. Huai, Thermal conductivity of single-walled carbon nanotubes under axial stress, *J. Phys. Chem. C* 114 (2010) 5786–5791.
- [37] R.D. Downes, A. Hao, J.G. Park, Y.F. Su, R. Liang, B.D. Jensen, E.J. Siochi, K.E. Wise, Geometrically constrained self-assembly and crystal packing of flattened and aligned carbon nanotubes, *Carbon* 93 (2015) 953–966.
- [38] W.J. Evans, M. Shen, P. Keblinski, Inter-tube thermal conductance in carbon nanotubes arrays and bundles: effects of contact area and pressure, *Appl. Phys. Lett.* 100 (2012) 261908.
- [39] A.N. Volkov, R.N. Salaway, L.V. Zhigilei, Atomistic simulations, mesoscopic modeling, and theoretical analysis of thermal conductivity of bundles composed of carbon nanotubes, *J. Appl. Phys.* 114 (2013) 104301.
- [40] L. Hu, A.J.H. McGaughey, Thermal conductance of the junction between single-walled carbon nanotubes, *Appl. Phys. Lett.* 105 (2014) 193104.
- [41] R.N. Salaway, L.V. Zhigilei, Thermal conductance of carbon nanotube contacts: molecular dynamics simulations and general description of the contact conductance, *Phys. Rev. B* 94 (2016) 014308.
- [42] M.J. Buehler, Mesoscale modeling of mechanics of carbon nanotubes: self-assembly, self-folding, and fracture, *J. Mater. Res.* 21 (2006) 2855–2869.
- [43] I. Ostanin, R. Ballarini, D. Potyondy, T. Dumitrică, A distinct element method for large scale simulations of carbon nanotube assemblies, *J. Mech. Phys. Solid.* 61 (2013) 762–782.
- [44] L.V. Zhigilei, C. Wei, D. Srivastava, Mesoscopic model for dynamic simulations of carbon nanotubes, *Phys. Rev. B* 71 (2005) 165417.
- [45] A.N. Volkov, L.V. Zhigilei, Mesoscopic interaction potential for carbon nanotubes of arbitrary length and orientation, *J. Phys. Chem. C* 114 (2010) 5513–5531.
- [46] S.W. Cranford, M.J. Buehler, In silico assembly and nanomechanical characterization of carbon nanotube buckypaper, *Nanotechnology* 21 (2010) 265706.
- [47] A.N. Volkov, L.V. Zhigilei, Structural stability of carbon nanotube films: the role of bending buckling, *ACS Nano* 4 (2010) 6187–6195.
- [48] A.N. Volkov, L.V. Zhigilei, Scaling laws and mesoscopic modeling of thermal conductivity in carbon nanotube materials, *Phys. Rev. Lett.* 104 (2010) 215902.
- [49] E.A. Colbourn (Ed.), *Computer Simulation of Polymers*, 1 ed., Longman, Harlow, 1994.
- [50] B. Xie, Y.L. Liu, Y.T. Ding, Q.S. Zheng, Z.P. Xu, Mechanics of carbon nanotube networks: microstructural evolution and optimal design, *Soft Matter* 7 (2011) 10039–10047.
- [51] C. Wang, B. Xie, Y.L. Liu, Z.P. Xu, Mechanotunable microstructures of carbon nanotube networks, *ACS Macro Lett.* 1 (2012) 1176–1179.
- [52] Y. Li, M. Kröger, A theoretical evaluation of the effects of carbon nanotube entanglement and bundling on the structural and mechanical properties of buckypaper, *Carbon* 50 (2012) 1793–1806.
- [53] Y. Li, M. Kröger, Computational study on entanglement length and pore size of carbon nanotube buckypaper, *Appl. Phys. Lett.* 100 (2012) 021907.
- [54] Y. Li, M. Kröger, Viscoelasticity of carbon nanotube buckypaper: zipping-unzipping mechanism and entanglement effects, *Soft Matter* 8 (2012) 7822–7830.
- [55] M.G. Hahm, H.L. Wang, H.Y. Jung, S. Hong, S.G. Lee, S.R. Kim, M. Upmanyu, Y.J. Jung, Bundling dynamics regulates the active mechanics and transport in carbon nanotube networks and their nanocomposites, *Nanoscale* 4 (2012) 3584–3590.
- [56] J.H. Zhao, J.W. Jiang, L.F. Wang, W.L. Guo, T. Rabczuk, Coarse-grained potentials of single-walled carbon nanotubes, *J. Mech. Phys. Solid.* 71 (2014) 197–218.
- [57] Y. Won, Y. Gao, M.A. Panzer, R. Xiang, S. Maruyama, T.W. Kenny, W. Cai, K.E. Goodson, Zipping, entanglement, and the elastic modulus of aligned single-walled carbon nanotube films, *Proc. Natl. Acad. Sci. U.S.A.* 110 (2013) 20426–20430.
- [58] L.V. Zhigilei, R.N. Salaway, B.K. Wittmaack, A.N. Volkov, Computational studies of thermal transport properties of carbon nanotube materials, in: A. Todri-Sanial, J. Dijon, A. Maffucci (Eds.), *Carbon Nanotubes for Interconnects: Process, Design and Applications*, Springer International Publishing, Cham, 2017, pp. 129–161.
- [59] Y.Z. Wang, C. Gaidau, I. Ostanin, T. Dumitrică, Ring windings from single-wall carbon nanotubes: a distinct element method study, *Appl. Phys. Lett.* 103 (2013) 183902.
- [60] I. Ostanin, R. Ballarini, T. Dumitrică, Distinct element method modeling of carbon nanotube bundles with intertube sliding and dissipation, *J. Appl. Mech.* 81 (2014) 061004.
- [61] P.A. Cundall, Formulation of a three-dimensional distinct element model—Part 1. A scheme to detect and represent contacts in a system composed of many polyhedral blocks, *Int. J. Rock Mech. Min. Sci.* 25 (1988) 107–116.
- [62] P.A. Cundall, O.D.L. Strack, Discrete numerical model for granular assemblies, *Geotechnique* 29 (1979) 47–65.
- [63] W.M. Jacobs, D.A. Nicholson, H. Zemer, A.N. Volkov, L.V. Zhigilei, Acoustic energy dissipation and thermalization in carbon nanotubes: atomistic modeling and mesoscopic description, *Phys. Rev. B* 86 (2012) 165414.
- [64] A.N. Volkov, T. Shiga, D. Nicholson, J. Shiomi, L.V. Zhigilei, Effect of bending buckling of carbon nanotubes on thermal conductivity of carbon nanotube materials, *J. Appl. Phys.* 111 (2012) 053501.
- [65] A.N. Volkov, L.V. Zhigilei, Heat conduction in carbon nanotube materials: strong effect of intrinsic thermal conductivity of carbon nanotubes, *Appl. Phys. Lett.* 101 (2012) 043113.
- [66] D.W. Brenner, Empirical potential for hydrocarbons for use in simulating the chemical vapor deposition of diamond films, *Phys. Rev. B* 42 (1990) 9458–9471.
- [67] D.W. Brenner, O.A. Shenderova, J.A. Harrison, S.J. Stuart, B. Ni, S.B. Sinnott, A second-generation reactive empirical bond order (REBO) potential energy expression for hydrocarbons, *J. Phys. Condens. Matter* 14 (2002) 783–802.
- [68] S.J. Stuart, A.B. Tutein, J.A. Harrison, A reactive potential for hydrocarbons with intermolecular interactions, *J. Chem. Phys.* 112 (2000) 6472–6486.
- [69] B. Bhushan, Nanotribology of carbon nanotubes, *J. Phys. Condens. Matter* 20 (2008) 365214.
- [70] O. Suekane, A. Nagataki, H. Mori, Y. Nakayama, Static friction force of carbon nanotube surfaces, *Appl. Phys. Express* 1 (2008) 064001.
- [71] S. Akita, Y. Nakayama, Interlayer sliding force of individual multiwall carbon nanotubes, *Jpn. J. Appl. Phys.* 42 (2003) 4830–4833.
- [72] T. Filleter, S. Yockel, M. Naraghi, J.T. Paci, O.C. Compton, M.L. Mayes, S.T. Nguyen, G.C. Schatz, H.D. Espinosa, Experimental-computational study of shear interactions within double-walled carbon nanotube bundles, *Nano Lett.* 12 (2012) 732–742.
- [73] J.T. Paci, A.O. Furmanchuk, H.D. Espinosa, G.C. Schatz, Shear and friction between carbon nanotubes in bundles and yarns, *Nano Lett.* 14 (2014) 6138–6147.
- [74] L.A. Girifalco, M. Hodak, R.S. Lee, Carbon nanotubes, buckyballs, ropes, and a universal graphite potential, *Phys. Rev. B* 62 (2000) 13104–13110.
- [75] B.K. Wittmaack, A.H. Banna, A.N. Volkov, L.V. Zhigilei, Mesoscopic modeling of structural self-organization of carbon nanotubes into vertically aligned networks of nanotube bundles, *Carbon* 130 (2018) 69–86.
- [76] D.N. Futaba, K. Hata, T. Yamada, T. Hiraoka, Y. Hayamizu, Y. Kakudate, O. Tanaike, H. Hatori, M. Yumura, S. Iijima, Shape-engineerable and highly densely packed single-walled carbon nanotubes and their application as super-capacitor electrodes, *Nat. Mater.* 5 (2006) 987–994.
- [77] S.J. Kang, C. Kocabas, T. Ozel, M. Shim, N. Pimparkar, M.A. Alam, S.V. Rotkin, J.A. Rogers, High-performance electronics using dense, perfectly aligned arrays of single-walled carbon nanotubes, *Nat. Nanotechnol.* 2 (2007) 230–236.
- [78] E. Einarsson, H. Shiozawa, C. Kramberger, M.H. Rummeli, A. Gruneis, T. Pichler, S. Maruyama, Revealing the small-bundle internal structure of vertically aligned single-walled carbon nanotube films, *J. Phys. Chem. C* 111 (2007) 17861–17864.
- [79] G.F. Zhong, J.H. Warner, M. Fouquet, A.W. Robertson, B.A. Chen, J. Robertson, Growth of ultrahigh density single-walled carbon nanotube forests by improved catalyst design, *ACS Nano* 6 (2012) 2893–2903.
- [80] G.H. Chen, Y. Seki, H. Kimura, S. Sakurai, M. Yumura, K. Hata, D.N. Futaba, Diameter control of single-walled carbon nanotube forests from 1.3–3.0 nm by arc plasma deposition, *Sci. Rep.* 4 (2014) 3804.
- [81] S.B. Hutchens, A. Needleman, J.R. Greer, Analysis of uniaxial compression of

- vertically aligned carbon nanotubes, *J. Mech. Phys. Solid.* 59 (2011) 2227–2237.
- [82] X.J. Liang, J.H. Shin, D. Magagnosc, Y.J. Jiang, S.J. Park, A.J. Hart, K. Turner, D.S. Gianola, P.K. Purohit, Compression and recovery of carbon nanotube forests described as a phase transition, *Int. J. Solid Struct.* 122 (2017) 196–209.
- [83] Information about the Comet supercomputer can be found by visiting <https://portal.xsede.org/sdsc-comet>.
- [84] J. Towns, T. Cockerill, M. Dahan, I. Foster, K. Gaither, A. Grimshaw, V. Hazlewood, S. Lathrop, D. Lifka, G.D. Peterson, R. Roskies, J.R. Scott, N. Wilkins-Diehr, XSEDE: accelerating scientific discovery, *Comput. Sci. Eng.* 16 (2014) 62–74.
- [85] H.J.C. Berendsen, J.P.M. Postma, W.F. Vangunsteren, A. Dinola, J.R. Haak, Molecular dynamics with coupling to an external bath, *J. Chem. Phys.* 81 (1984) 3684–3690.
- [86] S. Pathak, N. Mohan, E. Decolvenaere, A. Needleman, M. Bedewy, A.J. Hart, J.R. Greer, Local relative density modulates failure and strength in vertically aligned carbon nanotubes, *ACS Nano* 7 (2013) 8593–8604.
- [87] M. Alzaid, J. Roth, Y. Wang, E. Almutairi, S.L. Brown, T. Dumitrică, E.K. Hobbie, Enhancing the elasticity of ultrathin single-wall carbon nanotube films with colloidal nanocrystals, *Langmuir* 33 (2017) 7889–7895.
- [88] R. Richards Jr., *Principles of Solid Mechanics*, CRC Press, New York, 2000.
- [89] M.R. Maschmann, Q.H. Zhang, F. Du, L.M. Dai, J. Baur, Length dependent foam-like mechanical response of axially indented vertically oriented carbon nanotube arrays, *Carbon* 49 (2011) 386–397.
- [90] V.S. Deshpande, M.F. Ashby, N.A. Fleck, Foam topology bending versus stretching dominated architectures, *Acta Mater.* 49 (2001) 1035–1040.
- [91] M.F. Ashby, The properties of foams and lattices, *Philos. T. R. Soc. A* 364 (2006) 15–30.
- [92] A. Qiu, S.P. Fowler, J. Jiao, D. Kiener, D.F. Bahr, Time-dependent contact behavior between diamond and a CNT turf, *Nanotechnology* 22 (2011) 295702.
- [93] R. Thevamaran, F. Fraternali, C. Daraio, Multiscale mass-spring model for high-rate compression of vertically aligned carbon nanotube foams, *J. Appl. Mech.* 81 (2014) 121006.
- [94] M. Xu, D.N. Futaba, M. Yumura, K. Hata, Alignment control of carbon nanotube forest from random to nearly perfectly aligned by utilizing the crowding effect, *ACS Nano* 6 (2012) 5837–5844.
- [95] S.D. Mesarovic, C.M. McCarter, D.F. Bahr, H. Radhakrishnan, R.F. Richards, C.D. Richards, D. McClain, J. Jiao, Mechanical behavior of a carbon nanotube turf, *Scripta Mater.* 56 (2007) 157–160.
- [96] M.J. Buehler, Y. Kong, H.J. Gao, Deformation mechanisms of very long single-wall carbon nanotubes subject to compressive loading, *J. Eng. Mater. Technol.* 126 (2004) 245–249.
- [97] A. Sears, R.C. Batra, Macroscopic properties of carbon nanotubes from molecular-mechanics simulations, *Phys. Rev. B* 69 (2004) 235406.
- [98] N. Hu, K. Nunoya, D. Pan, T. Okabe, H. Fukunaga, Prediction of buckling characteristics of carbon nanotubes, *Int. J. Solid Struct.* 44 (2007) 6535–6550.
- [99] S. Adali, Variational principles for transversely vibrating multiwalled carbon nanotubes based on nonlocal Euler-Bernoulli beam model, *Nano Lett.* 9 (2009) 1737–1741.
- [100] S. Narendar, S.S. Gupta, S. Gopalakrishnan, Wave propagation in single-walled carbon nanotube under longitudinal magnetic field using nonlocal Euler-Bernoulli beam theory, *Appl. Math. Model.* 36 (2012) 4529–4538.
- [101] M.F. Ashby, *Materials Selection in Mechanical Design*, 5 ed., Elsevier, Boston, 2016.